Probing Phases of Quantum Matter with an Ion-Trap Tensor-Network Quantum Eigensolver

Michael Meth,[1,*] Viacheslav Kuzmin,[2,3,*] Rick van Bijnen,[2,3] Lukas Postler,[1] Roman Stricker,[1] Rainer Blatt,[1,3,4] Martin Ringbauer,[1] Thomas Monz,[1,4] Pietro Silvi,[1,5] and Philipp Schindler[1]

[1]*Institut für Experimentalphysik, Universität Innsbruck, Innsbruck, Austria*
[2]*Institut für Theoretische Physik, Universität Innsbruck, Innsbruck, Austria*
[3]*Institute for Quantum Optics and Quantum Information of the Austrian Academy of Sciences, Innsbruck, Austria*
[4]*Alpine Quantum Technologies GmbH, Innsbruck, Austria*
[5]*Dipartimento di Fisica e Astronomia, Università di Padova & INFN sezione di Padova, Padova, Italy*

(Received 8 April 2022; revised 15 October 2022; accepted 9 November 2022; published 27 December 2022)

Tensor-network (TN) states are efficient parametric representations of ground states of local quantum Hamiltonians extensively used in numerical simulations. Employing TN *Ansatz* states directly on a quantum simulator can potentially offer an exponential computational advantage over purely numerical simulation. We implement a quantum-encoded TN *Ansatz* state using a variational quantum eigensolver on an ion-trap quantum computer that approximates the ground states of the extended Su-Schrieffer-Heeger model. The generated states are characterized by estimating the topological invariants, verifying their topological order. Our TN encoding as a trapped-ion circuit employs only single-site optical pulses—the native operations naturally available on the platform. We reduce nearest-neighbor crosstalk by selecting different magnetic sublevels with well-separated transition frequencies to encode the qubits in neighboring ions.

DOI: 10.1103/PhysRevX.12.041035 Subject Areas: Quantum Physics

I. INTRODUCTION

Quantum phases of matter that do not have a classical counterpart, known as exotic phases, are pivotal in the development of novel quantum materials and devices [1,2]. Recently, topologically ordered phases have drawn much interest as potential fault-tolerant components for quantum technologies [3–5]. Yet, our understanding of such collective quantum phenomena remains incomplete [6]. While analytical treatment supports only a few (integrable) examples [7–9], numerical studies are limited to small systems due to the exponential growth of the state space in many-body quantum problems. Numerical approximations are thus used at intermediate and large systems. At these sizes, tensor-network (TN) methods provide a successful approach [10–12]. TN *Ansatz* states can efficiently represent ground states of bulk-gapped Hamiltonians in one and higher dimensions [13–15], including topological insulators [16,17]. In one spatial dimension, TNs—and matrix product states (MPSs) as a special case—are efficient when evaluating observables. However, numerical resources for exact evaluations in higher-dimensional TN states often increase exponentially in the system size. Various efficient approximation techniques are known [18,19], although the precision of these approaches is often not tunable.

Quantum simulators [20] provide an alternative pathway toward understanding many-body quantum phenomena. Recent progress in quantum hardware [21,22] enabled state-of-the-art experiments that are at the cusp of outperforming classical computers [4,23–34]. However, the current noisy intermediate-scale quantum (NISQ) devices [35] are still fairly limited, either by size, controllability, or noise. Quantum-classical algorithms, such as variational quantum eigensolvers (VQEs) [36–40], are protocols designed for NISQ devices [41] and, in the near term, have the potential to outperform either purely quantum or classical approaches. Such hybrid methods aim to solve problems where implementing a given computational task with specialized quantum resources can provide an advantage over the classical hardware. In this context, NISQ processors can be tailored to represent and sample TN states [42–49], e.g., by encoding specific classes of variational TNs as programmable quantum circuits. Said circuits thus allow the implementation of an efficient variational *Ansatz* used, for instance, in VQEs [38,39], to approximate ground states of local gapped Hamiltonians on a quantum simulator. While the observables (including the energy cost function) are measured directly on the

[*]These authors contributed equally to this work.

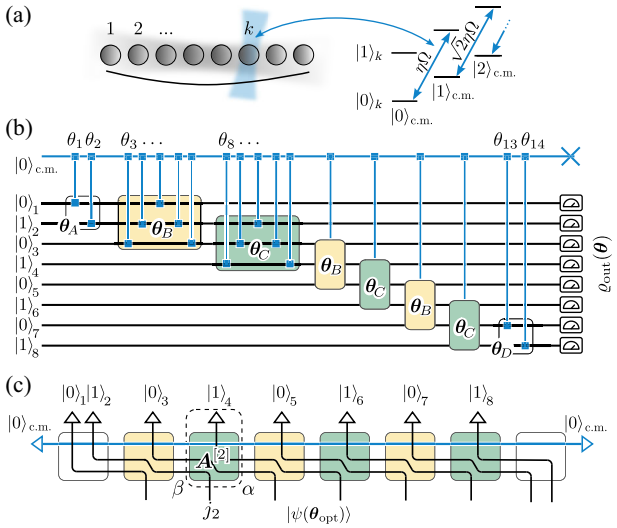

FIG. 1. Scheme of the TN VQE realized on a string of eight ions. (a) The logical states $|0\rangle_k$ and $|1\rangle_k$ are encoded in electronic levels of ion k. $|i\rangle_{\text{c.m.}}$ are the basis states of the bosonic axial center-of-mass (c.m.) phonon mode. We implement entangling operations (vertical blue lines) between a single qubit and the c.m. mode (blue horizontal line). (b) TN variational circuit built with blue-sideband operations as the only resource. (c) The resulting optimized many-body quantum state expressed in the graphical notation of tensor networks, which clearly highlights the bipartite entanglement distribution of a matrix product state. The empty triangles indicate contraction with pure single-qubit states written nearby. The dashed rounded rectangle indicates tensor $A^{[2]}_{j_2,\alpha,\beta}$, which is given by Eq. (5).

quantum device, the circuit parameters are optimized by a classical computer based on the respective measurement outcomes. This provides a potential computational advantage over purely classical approaches [50–52].

In the present work, we utilize trapped-ion quantum resources, sketched in Fig. 1(a), to implement a tensor-network-based VQE (TN VQE). Its purpose is to prepare a many-body entangled ground state on the ion qubits. As a variational resource, we use operations arising naturally in ion traps. The ions are sequentially interacting with a common motional (phonon) mode, which acts as an entanglement carrier [53–55] or quantum data bus (QDB), as highlighted in Fig. 1(b). In our approach, the interactions are optimized by a classical algorithm with the ultimate goal to realize a target many-body quantum state with the phonon mode being disentangled from the ions at the end of the circuit [46].

As a relevant target problem, we use our TN VQE to demonstrate topologically ordered ground-state phases in the nonintegrable extended Su-Schrieffer-Heeger (ESSH) model [56,57] shown in Fig. 2(a). The target states allow an accurate, efficient representation as MPSs since they are ground states of 1D gapped Hamiltonians [11,12,58]. We experimentally approximate the ground states of various model phases by running the TN VQE algorithm. Finally, we measure many-body topological invariants [57] (MBTIs) in the prepared states to detect phases and identify their topological order [59,60]; see Figs. 2(b) and 2(c).

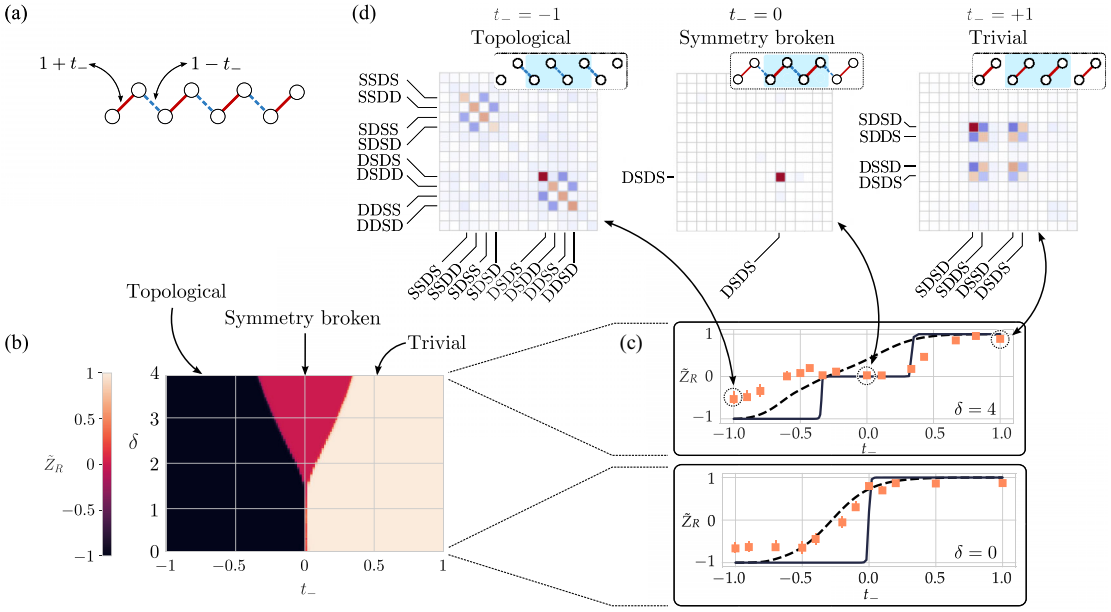

FIG. 2. (a) Sketch of the ESSH model for $N = 8$ sites, with neighboring sites connected by alternating coupling strengths $1 \pm t_-$ denoted by solid red and dashed blue bonds. (b) Partial-reflection MBTI $\tilde{Z}_R$ Eq. (7) calculated numerically for a system of infinite size $N \to \infty$ and $n = 100$ using the infinite-size density matrix renormalization group technique [11]; labels give the phases of the ESSH model. (c) Comparison of numerical values of MBTIs for a finite-sized system (dashed), the thermodynamic limit (solid), and the experimentally obtained data (square markers) for $\delta = 0$ (bottom) and $\delta = 4$ (top). (d) Real component of the reduced density matrices for the four central ions at $\delta = 4$ and $t_- \in \{-1, 0, +1\}$. The corresponding data points of $\tilde{Z}_R$ are indicated by arrows.

II. TENSOR-NETWORK VARIATIONAL QUANTUM EIGENSOLVER WITH TRAPPED IONS

In this section, we briefly review the concept of the TN VQE approach in trapped ions as previously proposed in Ref. [46]. Further details on our experimental implementation are provided in Sec. IV. A VQE is a protocol which aims to prepare ground states of interacting Hamiltonians on programmable quantum hardware, while mitigating the imperfections. A VQE can address Hamiltonians inaccessible for a given quantum platform and provide the best possible outcome for the available resources. However, identifying the best programmable resources accessible in a specific quantum platform, for a given task, determines the efficiency of the VQE.

As our platform, we consider a chain of N ions in a linear Paul trap as sketched in Fig. 1(a). For each site k, the qubit $(|0\rangle_k, |1\rangle_k)$ is encoded in a pair of electronic levels of the respective ion. The electronic levels can be controllably coupled to collective vibrational (phonon) modes of the ion chain. The entanglement among the ions is distributed by bosonic excitations of the phonon modes, which act as QDBs.

A successful approach to create entanglement in ion-trap quantum computers is the Mølmer-Sørensen (MS) gate, which simultaneously couples a set of target ions to the QDB via an off-resonant bichromatic light field [54,55]. Two schemes can be implemented: (i) in an adiabatic approach, phonons are excited only virtually [61], whereas the nonadiabatic approach (ii) actively excites the motional states and disentangles the qubits from the motion at discrete time intervals [62,63]. However, simultaneously addressing two or more qubits is prone to crosstalk, where unwanted spectator ions participate in the MS gate, introducing correlated errors in the system. In our work, we investigate alternative operations relying merely on single qubit operations, to implement a VQE in ion traps that can provide an advantage in the number of variational parameters while preserving the robustness of the circuit to decoherence. A comprehensive analysis comparing the MS-gate-based approach to our implementation is provided in Appendix A.

Here we consider elementary quantum-processing resources that couple qubits and a single phonon mode as a first-order process in η, thus actively creating entanglement between ions and phonons. In practice, we employ controlled quantum dynamics generated by the anti–Jaynes-Cummings Hamiltonian at any single site k,

$$H_k = i\eta\Omega(a\sigma_k^- - a^\dagger\sigma_k^+) \tag{1}$$

with Rabi frequency Ω, in the Lamb-Dicke regime. Here, $a^\dagger\sigma_k^+$ excites the qubit $|0\rangle_k \longmapsto \sigma^+|0\rangle_k = |1\rangle_k$ and simultaneously creates a phonon $|n\rangle \longmapsto a^\dagger|n\rangle = \sqrt{n+1}|n+1\rangle$, while $a\sigma_k^-$ does the opposite.

For optical qubits, such dynamics are realized by driving with blue-detuned local laser pulses in resonance with the motional sideband of a selected phonon mode [64] as sketched in Fig. 1(a). Here, we consider the axial center-of-mass (c.m.) mode due to the near homogeneous coupling to all ions in the chain, the large frequency gap to higher-order modes [65], and the geometry of the experimental setup, making it the most accessible mode. Originally, these sideband operations were proposed and used for implementing the controlled-NOT gate in trapped ions [53,66,67]. However, the accurate implementation requires precise calibration of the experimental setup as well as cooling of the phonon modes to zero temperature, as the effective Rabi frequency of the sideband operations heavily depends on the phonon population proportional to $\sqrt{n}$. Miscalibrations and any finite phonon population lead to imperfect gates, and, as a result, residual entanglement between the QDB and the qubits at the end of a circuit.

In our previous work [46], it was proposed to tackle this problem by employing adaptive feedback-loop strategies by a VQE in the presence of a quantum data bus [36–40]. For ion traps employing sideband operations, it was shown [46] that a VQE can suppress the detrimental impact of the finite motional temperatures. In Appendix A, we demonstrate the robustness to finite temperature and compare our approach directly to a VQE with MS gates. The goal is to prepare the pure ground state of a given Hamiltonian H_{targ} using the phonon mode as a data bus, which is required to be disentangled (only) at the end of the circuit. To this end, sideband operations are arranged to build a variational circuit $U(\boldsymbol{\theta}) = \prod_l \exp(-i\theta_l H_{k(l)})$, where the lth operation acts on the $k(l)$th ion, and the parameters $\boldsymbol{\theta} \equiv \{\theta_l\}$ are controlled by the durations of the laser pulses. For simplicity, let us consider the ideal case where the ions are initialized in some accessible pure state $|\psi\rangle_{\text{in}}$, and the QDB is prepared at zero temperature $|0\rangle_{\text{c.m.}}$, with $a|0\rangle_{\text{c.m.}} = 0$. Unlike a VQE in closed systems, the output variational states of the qubits

$$\rho_{\text{out}}(\boldsymbol{\theta}) = \text{Tr}_{\text{c.m.}}[U(\boldsymbol{\theta})(|\psi\rangle\langle\psi|_{\text{in}} \otimes |0\rangle\langle 0|_{\text{c.m.}})U^\dagger(\boldsymbol{\theta})] \tag{2}$$

are not restricted to pure states and are generally mixed due to residual ion-phonon entanglement at the end of the circuit. Nevertheless, the procedure to optimize the variational parameters is analogous to the standard VQE. Namely, we experimentally measure the energy

$$E(\boldsymbol{\theta}) = \text{Tr}[H_{\text{targ}}\rho_{\text{out}}(\boldsymbol{\theta})] \tag{3}$$

of the output state for the target model H_{targ} by evaluating all contributing observables. As usual, several experimental shots are required to evaluate the energy expectation value within a desired error bar [26]. The measured energy then acts as a cost function of a numerical variational optimizer, which iteratively proposes new parameter sets $\boldsymbol{\theta}$ to find a

global minimum in the landscape of the variational *Ansatz* manifold. The optimization algorithm we employ is discussed in detail in Sec. V. Upon convergence to the ground-state energy, for some optimal parameters $\boldsymbol{\theta}_{\text{opt}}$, the prepared state $\rho_{\text{out}}(\boldsymbol{\theta}_{\text{opt}})$ approaches the manifold of (nearly) degenerate ground states. If the ground state is unique, then $\rho_{\text{out}}(\boldsymbol{\theta}) = |\psi(\boldsymbol{\theta}_{\text{opt}})\rangle\langle\psi(\boldsymbol{\theta}_{\text{opt}})|$; thus, qubits are disentangled from the QDB at the end of the preparation. At this optimal scenario, our circuit *Ansatz* guarantees [42] that the optimized output state can be represented as

$$|\psi(\boldsymbol{\theta}_{\text{opt}})\rangle = \sum_{j_1,\ldots,j_N} \boldsymbol{A}^{[1]}_{j_1},\ldots,\boldsymbol{A}^{[N]}_{j_N}|j_1,\ldots,j_N\rangle, \tag{4}$$

as sketched graphically in Fig. 1(c) [46]. Here, $j_k \in \{0,1\}$ are indices of the canonical basis of the kth qubit, and $\boldsymbol{A}^{[k]}_0$, $\boldsymbol{A}^{[k]}_1$ are $D_k \times D_{k+1}$ parametric matrices which correspond to the circuit. For example, the elements of matrix $\boldsymbol{A}^{[2]}_{j_2}$ are

$$A^{[2]}_{j_2,\alpha,\beta} = \langle j_2|\langle\alpha_{3,4,\text{c.m.}}|U_{2,3,4,\text{c.m.}}(\boldsymbol{\theta}_C)|\beta_{2,3,\text{c.m.}}\rangle|1_4\rangle. \tag{5}$$

Here the unitary [colored green in Fig. 1(b)] acts on the c.m. mode, and the qubits 2–4 as indicated by the lower indices and $|\beta_{2,3,\text{c.m.}}\rangle$ and $|\alpha_{3,4,\text{c.m.}}\rangle$ are the corresponding joint basis states. In this sense, the sizes D_k (rows) and D_{k+1} (columns) of the matrices $\boldsymbol{A}^{[k]}_j$ are effectively determined by the circuit design [46]. Figure 1(c) shows exactly how the circuit can be graphically reshaped into a matrix product state using the standard graphical notation of tensor networks: Solid lines represent quantum degrees of freedom (black, qubit; blue, phonon mode), and they can interact only while they are within the same box.

The states described by Eq. (4) are MPSs [42,68], and the bond dimension $D = \max_k D_k$ is the "refinement parameter" of the *Ansatz*: In numerical simulations, this integer value controls the degree of approximation and complexity of the algorithm and approaches exact diagonalization in both precision and costs in the limit $D \to \infty$. The entanglement entropy of the real-space bipartitions in the MPS is bounded as $s \leq \log D$ matching the area law of entanglement for the ground states of gapped 1D Hamiltonians [69]. Indeed, it was shown that a MPS provides an efficient and faithful *Ansatz* to approximate such states [11,12,58]. In our circuit, D is controlled by the lattice size m of the sideband operation blocks (colored boxes in Fig. 1), such that $D \lesssim 2^{m-1}$.

Additionally, typical quantum lattice Hamiltonians exhibit translational invariance; namely, they can be formally decomposed as $H_{\text{targ}} = \sum_k h_k$ while satisfying $h_k = h_{k+\ell}$, which represents a period of ℓ lattice sites labeled by k. Ground states of translation-invariant Hamiltonians are well approximated by bulk-translation-invariant MPSs with tensors $\boldsymbol{A}^{[k]}_{j_k} = \boldsymbol{A}^{[k+\ell]}_{j_{k+\ell}}$ in the bulk. In our circuit, this can be achieved by repeatedly using the same subset of variational parameters along the circuit with period ℓ: In the language of Fig. 1, boxes of the same color use the same parameters. The optimal size of the edge blocks with the unique parameters can be identified variationally in the experiment, and it is expected to grow solely with the quantum correlation length of the target state. Consequently, the number of independent scalar parameters in the circuit *Ansatz* does not ultimately grow for increasing system size.

III. TARGET MODEL

We use a TN VQE in an ion trap to study phases in the interacting extension of the Su-Schrieffer-Heeger model [70,71], a one-dimensional spin-chain Hamiltonian capturing the transport properties of polymer molecules [72]. Open-boundary conditions are required to exhibit topological order, and the Hamiltonian for N sites reads

$$H_{\text{ESSH}} = \sum_{k=1}^{N-1}[t_+ + (-1)^{k-1}t_-] \times (\sigma^x_k\sigma^x_{k+1} + \sigma^y_k\sigma^y_{k+1} + \delta\sigma^z_k\sigma^z_{k+1}) \tag{6}$$

in dimensionless units, where σ^μ_k are the Pauli operators acting on qubit k. In the following, we fix the coupling $t_+ = 1$. The coupling t_- controls the "staggerization" of the interaction strength, separating even-odd from odd-even pairs as sketched in Fig. 2(a). Additionally, δ defines the anisotropy of the XXZ-type interaction, and the "standard" SSH model [56] coincides with the case $\delta = 0$. For $\delta \neq \{0,1\}$, the model is not integrable, thus requiring numerical techniques to study its behavior. In the antiferromagnetic regime ($\delta \geq 0$), the model exhibits three different energy-gapped phases at zero temperature [57], as indicated in Fig. 2(b): (i) a nondegenerate trivial dimer phase, (ii) a fourfold (quasi) degenerate symmetry-protected topological (SPT) dimer phase with soft excitations localized at the edges, and (iii) a spontaneously symmetry-broken, Ising antiferromagnetic phase emergent at large δ.

The transition between symmetry-protected topologically ordered phases can be detected using many-body topological invariants [59,60] associated with the symmetries protecting the corresponding phases of the 1D system. In the case of the ESSH model, these symmetries [73,74] are the dihedral group of π rotations about two orthogonal axes, reflection symmetry with respect to the center of the bond, or time-reversal symmetry. In the present work, we consider the partial-reflection and the partial-time-reversal MBTIs [60] corresponding to the two last symmetries. Each of the MBTIs can be used as a separate phase detector. The partial-reflection MBTI reads [57,60]

$$\tilde{Z}_R = \frac{\mathrm{Tr}[\rho_I \hat{R}_I]}{\sqrt{(\mathrm{Tr}[\rho_{I_1}^2] + \mathrm{Tr}[\rho_{I_2}^2])/2}}. \quad (7)$$

Here, ρ_I, ρ_{I_1}, and ρ_{I_2} are reduced states of subsystems $I = I_1 \cup I_2$, where I includes an even number $n < N$ of sites in the middle, and I_1 and I_2 are their left and right subsystems. The parity operator $\hat{R}_I = \hat{R}_I^\dagger = \hat{R}_I^{-1}$ reflects the 1D lattice around its center, practically swapping each symmetric pair of qubits. Analogously, the time-reversal MBTI [57,60] is

$$\tilde{Z}_T = \frac{\mathrm{Tr}[\rho_I u_T \rho_I^{T_1} u_T^\dagger]}{[(\mathrm{Tr}[\rho_{I_1}^2] + \mathrm{Tr}[\rho_{I_2}^2])/2]^{3/2}}, \quad (8)$$

where T_1 indicates the partial transpose operation on the partition I_1, and $u_T = \prod_{i \in I_1} \sigma_i^y$, so that the antiunitary mapping $\rho_I \to u_T \rho_I^{T_1} u_T^\dagger$ completely inverts the spin (thus, time reversal) of each qubit inside I. In the thermodynamic limit, with $N \gg n \to \infty$ (both N and n being multiples of 4), $\tilde{Z}_R$ and $\tilde{Z}_T$ approach discrete values in the gapped phases, as demonstrated in Figs. 2(b) and 2(c). In this sense, they are actual invariants; i.e., their experimentally observed values are insensitive to any local fluctuation, which does not disrupt the SPT symmetry. This property confirms that $\tilde{Z}_R$ and $\tilde{Z}_T$ are proper topological phase indicators characterizing the topological content even when there are residual (local, non-SPT-breaking) quasiparticle excitations in the system.

Precisely, the MBTIs acquire the value $\tilde{Z}_R = \tilde{Z}_T = 1$ in the trivial phase, -1 in the topological phase, and 0 in the symmetry-broken phase, respectively. The subsystem size n required to achieve the convergence depends on the correlation length in the system [57]. Thus, in the finite-size system, the measured MBTIs become smoothed in proximity of phase boundaries, as shown in Fig. 2(c) for $\tilde{Z}_R$, where we take $N = 8$ and $n = 4$. While reconstructing the estimators Eqs. (7) and (8) has a measurement cost that scales exponentially with the bulk size n, we stress that the MBTIs are expected to converge rapidly, in n, to values which can clearly discriminate between the topologically ordered phases [59].

Far from the phase boundaries, the ESSH ground states are gapped phases satisfying the entanglement area law [14,15], and thus allowing an efficient MPS representation that can be realized with TN VQE. Notably, blue-detuned sideband (BSB) operations of Eq. (1) are a sufficient resource to prepare ground states of any real, z-magnetization-conserving Hamiltonian [46]. Moreover, these operations take into account specific symmetry properties of H_{ESSH}, eventually simplifying the optimization problem within TN VQE. Precisely, due to its symmetries, H_{ESSH} always exhibits at least one ground state with zero z magnetization and all real amplitudes in the canonical basis. Accordingly, BSB operations realize real-valued variational unitaries $U(\boldsymbol{\theta})$ since the H_k are fully imaginary. Furthermore, they protect an "extended" magnetization symmetry $1/2 \sum_k \sigma_k^z - a^\dagger a$. Thus, if the initial qubit state has well-defined z magnetization, so does the output qubit state once the c.m. mode has been variationally disentangled [46]. Thus, by protecting these two symmetries (magnetization, complex conjugation), which are present in the target model, we substantially simplify the variational optimization problem [26]. Conversely, we cannot protect the symmetry-protected topologically ordered symmetries (reflection, time reversal, etc.): doing so would prevent us from establishing topological order from a trivial input state.

IV. EXPERIMENTAL IMPLEMENTATION

We implement a TN VQE on an ion-trap quantum simulator using laser-cooled $^{40}Ca^+$ ions in vacuum [75]. All experimental results presented here are carried out on linear strings of eight ions. We encode the qubits in the optical transitions from the electronic ground state $4S_{1/2}$ to the $3D_{5/2}$ manifold, such that $|0\rangle = |4S_{1/2}\rangle$ and $|1\rangle = |3D_{5/2}\rangle$. The $3D_{5/2}$ state is long-lived with a lifetime of $T_1 = 1.15$ s. The system is prepared in the electronic and motional ground state by a sequence of Doppler-, polarization-gradient, and sideband-cooling and optical pumping [75]; we achieve a mean phonon number $\bar{n} \leq 0.05$.

The quantum state of each qubit is manipulated by a sequence of laser pulses. For each circuit, we aim to implement the sideband operations Eq. (1) on a single qubit at a time, requiring precise control over the position of the laser beam [76,77]. In our setup, we address the ions individually via a high numerical aperture objective aligned at an angle of 22.5° with respect to the ion string axis. Such single-qubit operations will inevitably introduce crosstalk errors in the nonaddressed ions. Because of the geometry of the laser beam, a finite residual field will overlap with—most prominently—immediate neighbors, inducing excess rotations and phase errors [78]. Comparing the Rabi frequency Ω_j of a target qubit on site j with its neighbors $j \pm 1$, we measure the ratio $\Omega_{j\pm1}/\Omega_j$ to be as large as 5.9 (5)% in the center of the ion string, which corresponds to a relative laser intensity of 0.35%.

We seek to minimize the crosstalk errors arising during state preparation and measurement via two schemes. First, resonant errors on the $|S\rangle \leftrightarrow |D\rangle$ carrier transition are suppressed by implementing a sequence of qubit rotations, decoupling the spectators from the target ion j. Here, any rotation $\tilde{R}_j$ of the qubit by the Euler angles θ, ϕ, and λ on the Bloch sphere is decomposed into a set of single-qubit rotations

$$\tilde{R}_j(\theta, \phi, \lambda) = Z_j(\phi) X_j(\pi/2) Z_j(\theta) X_j(-\pi/2) Z_j(\lambda), \quad (9)$$

where X_j rotates the state vector about the x axis and Z_j about the z axis [79]. We implement X_j by resonantly driving the carrier transition, while Z_j is realized by a far-detuned laser pulse inducing an ac Stark shift, in turn rotating the state of the qubit in the equatorial plane of the Bloch sphere. Since the ac Stark shift is proportional to the intensity of the laser rather than the amplitude, as in the case of the resonant transition, the crosstalk is suppressed quadratically. Thus, resonant crosstalk can be attributed to the X operations in the sequence in Eq. (9) alone, and as both of them are subjected to the same systematic errors, any resonant error is canceled out by the opposing phase angles. With this method, we manage to suppress resonant crosstalk to well below 1%. Alternatively, the $Z_j(\theta)$ operations could be implemented virtually by increasing the local phase reference of the addressed qubit [80]. However, we do not resort to this scheme, as our setup allows us to achieve resonant single-qubit gate fidelities beyond 99.9% and are thus negligible in the context of state preparation and measurement. However, the decoupling scheme we describe is not applicable when driving sideband operations. First, the Stark shift experienced by the individual states depends on the phonon occupation n [81]. Second, the effective Rabi frequency scales as $\sqrt{n}$, yielding a different evolution for each state. Here we implement a novel scheme using the internal structure of ^{40}Ca: We encode the qubit in different, spectrally well-separated transitions in the $4S_{1/2}$ and $3D_{5/2}$ manifolds; specifically, we select two transitions with magnetic quantum numbers $m = \pm 1/2$ as shown in Fig. 3. Thus, for a given site k, the encoding is defined as $|0\rangle = |4S, m = (-1)^k 1/2\rangle$ and $|1\rangle = |3D, m = (-1)^k 1/2\rangle$, respectively. This method prevents any unwanted sideband excitation on neighboring ions. However, it introduces additional efforts during state preparation. For each ion required to be initialized in the $|4S, m = +1/2\rangle$ ground state, two additional laser pulses would be needed. Conveniently, as our circuits start out from a Néel state $|0101\ldots\rangle$, we initialize $|3D, m = +1/2\rangle$ on all even sites where only a single pulse on the transition $|4S, m = -1/2\rangle \leftrightarrow |3D, m = +1/2\rangle$ is required for each respective site. We quantify the benefits of this scheme via state tomography of a circuit with $M = 14$ sideband operations on four qubits using parameters optimized in numerical simulation given in Appendix C and compare the data with the state obtained by the circuit simulation. We achieve a fidelity of $\mathcal{F} = 89.7(11)\%$ compared to 82.5(12)% in the case with all qubits encoded in the $|4S, m = -1/2\rangle \leftrightarrow |3D, m = -1/2\rangle$ transition. Assuming the state fidelity is described by $\mathcal{F} = (\mathcal{F}_{\mathrm{BSB}})^M$, the fidelity of a single BSB operation is given by $\mathcal{F}_{\mathrm{BSB}} = 99.23(7)\%$.

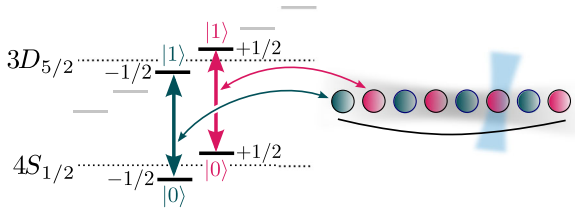

FIG. 3. Crosstalk suppression by staggered encoding of qubits in different, well-separated Zeeman transitions. For a given site k, the qubit is implemented in the $|4S, m = (-1)^k 1/2\rangle \leftrightarrow |3D, m = (-1)^k 1/2\rangle$ transition.

Apart from state preparation and measurement, the full circuit is implemented using only single-ion sideband operations. In these operations, the phonon-ion coupling scales with the Lamb-Dicke parameter η, which heavily depends on the trap geometry, or more precisely, on the overlap of the incident laser beam and the trap axis. In our setup, we measure $\eta = 0.038$, implying a requirement of up to 2 mW of peak laser power to implement the sideband operations, which in turn induce ac Stark shifts Δ by coupling to the carrier transition with a strength on the order of $\Delta \approx 5$ kHz. These shifts are actively compensated by a second, far detuned laser beam [82]. Since this requires substantial power in the compensation beam and with the total available laser power being finite, the achievable Rabi frequency is also limited. We find the optimum to be at a sideband coupling strength of $\eta\Omega = 2\pi \times 8$ kHz, such that a π rotation $|0, n = 0\rangle \leftrightarrow |1, n = 1\rangle$ is performed in approximately 125 μs.

In contrast to other entangling schemes like the MS gate [54], the sideband operations executed in our circuits actively entangle the ions with the phonon mode. Uncontrollable interactions with the environment cause the qubits to depolarize, mainly due to heating and motional dephasing as a consequence of, predominantly, electric field noise in the trap [83]. In our setup, we measure the heating rate of $\Gamma_H = 27(2)$ phonons per second in an eight-ion crystal. Furthermore, we measure the motional coherence time $\boldsymbol{\tau_{\mathrm{c.m.}}}$ of the c.m. mode via Ramsey spectroscopy. For a single qubit, we obtain $\tau_{\mathrm{c.m.}} = 101.9(1)$ ms, which is comparable to the coherence time of the laser given by $T_2 = 107(15)$ ms. However, the motional coherence time will decrease with the number of ions in the trap. On an eight-ion string, we measure $\tau_{\mathrm{c.m.}} = 21.9(2)$ ms, which is by a factor of 5 lower than T_2. As such, we identify heating and motional dephasing as our main decoherence mechanisms. Consequently, in our setup, it is paramount that each sideband sequence is finished well within the characteristic times $\tau_H = 1/\Gamma_H$ and $\tau_{\mathrm{c.m.}}$ to ensure the faithful implementation of the target state.

A. Toward 2D geometries

The design of our experiment focuses on the ground-state approximation of a one-dimensional model by exploiting the properties of MPSs. However, it is important to highlight that the ultimate goal of the TN-VQA method is to efficiently reconstruct—on a hybrid quantum simulator—equilibrium states of many-body Hamiltonians

in two or higher spatial dimensions. In fact, while MPSs allow for an accurate, efficient algorithm to numerically simulate 1D ground states, such as the density matrix renormalization group (DMRG) [84,85], their two-dimensional counterpart (the projected entangled-pair states, PEPSs) [86,87] is not exactly contractible, and their expectation values are typically computed through uncontrolled approximations [18]. Thus, being able to experimentally construct tensor-network variational states for two-dimensional lattices allows us to circumvent the limitation of numerical simulations via hybrid quantum algorithms. The past few years gave rise to a variety of proposals for experimental realization of a TN VQE to study 2D lattice systems [43,88–91]. In particular, recent work [91] discusses quantum circuits for sequential generation of plaquette PEPS—a subclass of PEPS [86,87]—that is believed to include a large class of 2D phases, including the topological ones [89]. Some of the proposed experimental realizations [92] in circuit quantum electrodynamics (QED) could in principle be translated on ion-trap platforms, provided it is possible to measure and reset individual ions while preserving coherence in the rest of the system [93]. The technique demonstrated in the present work can be used to implement local "plaquette" unitaries required to entangle the emitters with ancillas. We speculate on how to build such an experimental tensor-network state—albeit with resources that may be available in the near future—and detail the strategy in Appendix E.

V. VARIATIONAL OPTIMIZATION

The objective of our variational quantum eigensolver is to prepare the many-body ground state of the target Hamiltonian H_{ESSH} of Eq. (6) via closed-loop optimization. For a given set of couplings $t_- \in [-1, 1]$ and $\boldsymbol{\delta} > \mathbf{0}$, the protocol proposes sets of trial parameters $\boldsymbol{\theta}$ and evaluates the energy functional

$$E(\boldsymbol{\theta}) = \mathrm{Tr}\{\rho_{\mathrm{out}}(\boldsymbol{\theta}) H_{\mathrm{ESSH}}\} \tag{10}$$

via data obtained directly on the ion-trap quantum simulator. A simplified sketch highlighting the full VQE is shown in Fig. 4(a). For each parameter set $\boldsymbol{\theta}$, we implement the circuit Fig. 1(b) and measure collectively in the X, Y, and Z basis. The measurement outcome is then fed back to the classical computer, which evaluates Eq. (10) and makes an improved guess for new input parameters, thus iteratively minimizing $E(\boldsymbol{\theta})$.

The classical optimization algorithm that minimizes the energy functional over the parameters $\boldsymbol{\theta}$ is based on the pattern search algorithm [94,95]. This local search algorithm moves around in parameter space by polling nearby points to a candidate solution $\boldsymbol{\theta}_c$. The polling points are organized according to a stencil centered at the candidate solution and comprised of orthogonal vectors in each of the possible search directions. Based on the experimentally

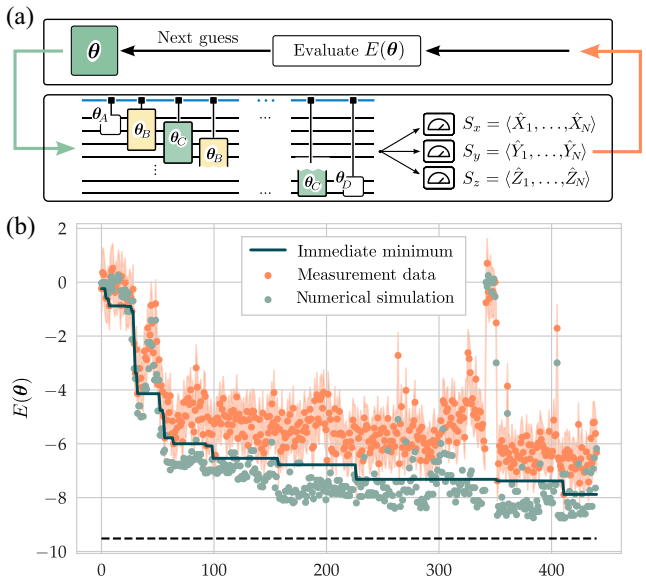

FIG. 4. (a) Sketch of the VQE protocol. (b) Energy $E(\boldsymbol{\theta})$ of the prepared variational states $|\Psi(\boldsymbol{\theta})\rangle$ for $t_- = \delta = 0$ during closed-loop optimization; errors are calculated considering shot noise and are shown as error bars. For each step, we show the immediate minimum that is reached thus far by a solid line; the energy of the exact ground state is shown as dashes. The numerical data are derived from simulations of the circuits for the respective parameters $\boldsymbol{\theta}$.

measured cost function values sampled at each of the polling points, the algorithm decides to move the stencil to a new candidate solution $\boldsymbol{\theta}_{c+1}$. If none of the polling points provides an improvement, the size of the stencil is decreased. Contrarily, upon a successful energy-lowering move, the stencil size is increased. The stencil is rotated such that the first polling vector is oriented along the direction of the last successful move.

Since the cost function landscape is sampled only through noisy projective measurements, some additions to the algorithm are made. First, a Gaussian process model [96] is fitted to the data to provide a better estimate of the cost function in the neighborhood of the current candidate point. This is to be compared with standard gradient-based algorithms that fit a linear model to the locally obtained function values and move the candidate solution accordingly. Here instead, we fit a global model, taking into account all previous measurement outcomes. A second modification for dealing with noisy cost function values is the option for the algorithm to request additional samples at already polled points in cases where the error bars on the energy estimates are deemed too large to be able to make a good decision on where the stencil should be moved. In this refinement step, elements of optimal computational budget allocation are employed [97].

We now briefly discuss details related to the implementation in the experiment. Each set of trial parameters $\boldsymbol{\theta}$ is defined by 14 individual angles θ_k in units of π, which are

transpiled into a sequence of sideband operations adhering to the proposed pattern in Fig. 1(b) [46]. However, the experimental setup imposes a lower limit on the θ_k. While we are able to electronically control the pulse duration with a step size of 8 ns, adiabatic amplitude shapes reducing off-resonant carrier excitations set the minimum pulse duration with some margin allowing the electronics to properly execute the signal to 10 μs [98,99]. As such, small rotations are automatically dropped by the transpiler. With a target Rabi frequency of $\Omega \approx 2\pi \times 8$ kHz, this pulse length translates into an angle approximately equal to 0.03π. Thus, the actual circuit might differ from Fig. 1(c). Nevertheless, simulations show that such small angles have negligible impact on the implemented quantum state.

An example of the closed-loop optimization presenting real data for the parameters $t_- = 0$ and $\delta = 0$—the critical point in the thermodynamic limit—is shown in Fig. 4(b). Starting with an initial guess $\boldsymbol{\theta} = \{0\}$, the algorithm evaluates Eq. (10) for each optimization step. The solid line indicates the minimum for $E(\boldsymbol{\theta})$ in the experimental data achieved thus far. For comparison, we show the value from numerical simulations of the circuit for each of the proposed parameter sets. We show our "best guess" reaching $E(\boldsymbol{\theta}_{\text{opt}}) \approx -8$ compared to the exact value of $E_{\text{min}} = -9.52$.

VI. RESULTS

In this section, we present the experimental verification of different phases in the ESSH model by means of many-body topological invariants as phase detectors. For each dataset, we first run the variational optimization algorithm and, upon convergence, obtain an optimal parameter set $\boldsymbol{\theta}_{\text{opt}}$. In our experiment, the quantum state of the bulk region, i.e., the four-ion state $\rho_{3,4,5,6}$ in the center of the string, as shown in Fig. 2(d), is measured via full state tomography and reconstructed using maximum-likelihood methods [100,101]. We calculate the MBTIs $\tilde{Z}_R$ and $\tilde{Z}_T$ according to Eqs. (7) and (8) from the reconstructed density matrices and calculate the measurement errors via bootstrapping with 100 repetitions for each coupling strength t_-. We also compare the experimental results with (i) the target values from the exact finite-size ground states, (ii) values from a ground state close to the thermodynamic limit, and (iii) values from the states obtained by numerically simulating the circuits with the experimentally obtained optimal parameters $\boldsymbol{\theta}_{\text{opt}}$.

First, we discuss the case $\delta = 0$, where Eq. (6) is equivalent to the plain SSH model. In the thermodynamic limit, the transition between the topological and trivial phases occurs with increasing t_- at $t_- = 0$ and is indicated by the abrupt change of the MBTI values from -1 to 1, as given by solid black lines in Fig. 5. However, in the finite-size ground states, the MBTIs shown by dashed black lines change smoothly. Moreover, the center of the slope is shifted from $t_- = 0$ to the negative values due to finite-size

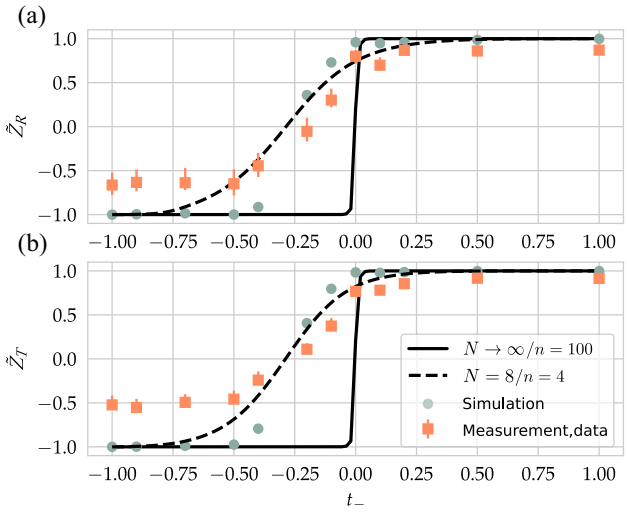

FIG. 5. Many-body topological invariants $\tilde{Z}_R$ (spatial reflection) and $\tilde{Z}_T$ (time reversal) with $N = 8$ and $n = 4$ in the ESSH model for $\delta = 0$ as a function of t_-. For comparison, a simulation of the input parameters $\boldsymbol{\theta}_{\text{opt}}$ is included together with $\tilde{Z}_{R/T}$ for the ground states in the thermodynamic limit $N \to \infty$ found by infinite-size density matrix renormalization group, and the finite system with $N = 8$.

effects, and specifically, that the number of odd-even terms in the ESSH Hamiltonian, Eq (7) dominates the number of even-odd terms by one.

The data obtained in our experiment shown by orange square markers are in good agreement with the described behavior and clearly demonstrate the transition of the MBTIs from the negative values in the topological phase to the positive in the trivial phases. We observe the most pronounced deviation of the experimental values from the target values and from the numerical simulation in the topological phase, especially with respect to the time-reversal symmetry in Fig. 5(b). This observation is attributed to decoherence processes in the c.m. mode and residual Stark shifts resulting in depolarization of the prepared states along the quantization axis of the qubits, which both MBTIs are sensitive to. A more detailed simulation analysis of this qualitative argument is included in Appendix B. Considering the example states shown in Fig. 2(d), it can be shown that both the MBTIs are quite fragile under dephasing in the topological phase, while they are relatively robust in the trivial phase (see also Appendix D). This effect is due to the algebraic properties of the MBTI itself, given that we consider a bulk of four sites. In fact, in the topological phase, losing coherences can cause $\tilde{Z}_R$ to increase all the way up to zero. Conversely, in the trivial phase, $\tilde{Z}_R$ can decrease only to $1/\sqrt{2}$. Such an asymmetry is reflected in the quality of the MBTIs in either phase.

Having explored the integrable case, we now consider the case $\delta = 4$, which exhibits the symmetry-broken phase (an Ising antiferromagnet) between the topological and

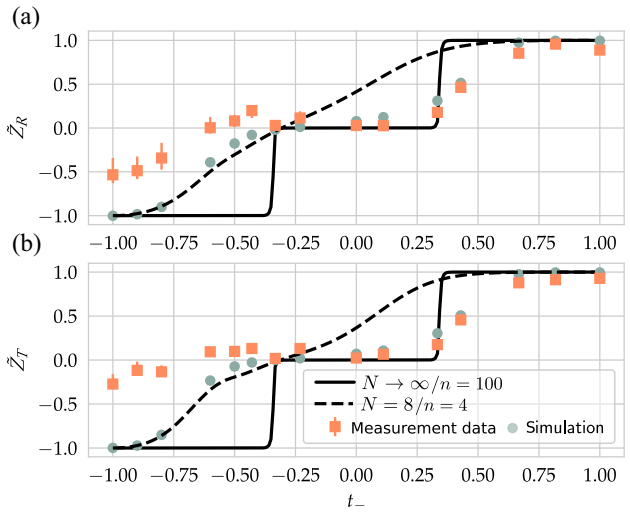

FIG. 6. MBTIs $\tilde{Z}_R$ and $\tilde{Z}_T$ in the ESSH model for $\delta = 4$, indicating a symmetry-broken phase in the region near $t_- \approx 0$. The notations are the same as in Fig. 5.

trivial phases due to the sharp anisotropy favoring interactions in the z direction. This phase is indicated by the abrupt change of the MBTIs to zero, as shown in Fig. 6. However, the exact finite-size ground state indicates almost no presence of the symmetry-broken phase. Interestingly, the symmetry-broken phase can be clearly observed from the experimental data. We attribute this behavior to the fact that at a finite size, the exact model resolves the ground-state degeneracy, and, in the finite-size unique ground state, the parity symmetry is not spontaneously broken. In contrast, due to imperfections and noise, the experimental VQE polarizes into a physical ground state with spontaneous symmetry breaking; see middle panel in Fig. 2(d). This state is less entangled, has smaller finite-size effects, and is thus closer to the values of the thermodynamic limit. For more details, see Appendix B. Similar to the case $\delta = 0$, we also observe deviation of the experimental values from the target values in the topological phase.

Despite the fragility of the MBTI in the presence of noise, the topological phase is well separated from the symmetry-broken phase. We compare the outcomes for $\tilde{Z}_T$ deep in the topological regime at $t_- = -1$ with the data at $t_- = 0$; here, we find a deviation of more than 6 standard deviations, which supports our claim of being able to resolve the individual phases in the SSH and ESSH model.

VII. CONCLUSIONS AND OUTLOOK

In the present work, we implement a variational quantum eigensolver in an ion-trap quantum device capable of targeting tensor-network states. We demonstrate that our technique is efficient at approximating entangled ground states of gapped Hamiltonians, including symmetry-protected topological phases. Our strategy encodes the tensor-network variational *Ansatz* in a quantum circuit which explicitly includes the c.m. vibrational mode as an entanglement mediator. The native interactions of the ions with the c.m. mode are used in our circuit as variational resource operations, and the target pure state is approximated in ions via a variational quantum eigensolver. We carry out our experiments in traps with eight ions and successfully approximate each gapped phase of the non-integrable interacting extension of the SSH model.

We view our work as a first step to realize a scalable tensor-network simulator on an ion-trap platform. The quality of our experiment is improved by spectroscopic decoupling to suppress crosstalk between the ions—one of the major imperfections in ion traps. We observe that one of the limitations on the system size N in our circuit is the finite coherence time $\tau_{\text{c.m.}}$ of the c.m. mode. Since the coherence time $\tau_{\text{c.m.}}$ of the c.m. mode scales as $1/N$ and with the Rabi frequency on the blue sideband decreasing as $1/\sqrt{N}$, one can estimate the error probability for a single variational block in first order to grow as $p \propto N^{3/2}$. As the c.m. is impacted the most by decoherence, working with higher-order motional modes which exhibit longer coherence times can overcome this limitation. However, this will require careful selection of said modes for each variational block, such that all qubits couple approximately equally to the motion. This in turn induces significant experimental overhead, mainly due to ac Stark shifts arising from the blue-sideband operations, requiring different compensation parameters for each qubit and mode. In more complex schemes, one could tailor local phonon modes using optical tweezers [102,103], which is beyond of the capabilities of our setup.

Longer circuits can be realized with several sideband sequences separated by intermediate recooling of the phonon mode in order to counteract heating. Such a scheme would require the qubits to be variationally disentangled from the phonon mode before each cooling step to guarantee that the qubit state is not impacted by decoherence introduced by the cooling itself. Whether the TN VQE algorithm would still work according to the same design, or if it would require a different protocol, needs to be investigated.

Our TN circuit employs translation invariance in the bulk; thus, we expect that the complexity of the optimization problem will not increase with the system size but only with the entanglement growth in the target state. Another challenge for large-scale simulation of many-body phases is their verification. In ion traps, this problem can be tackled by adapting randomized measurement techniques [52,57,104,105].

We discuss the fundamental role of extending the TN VQE toward 2D lattice systems [43,89–91] and tensor-network geometries for 2D, such as PEPSs [86,87]. In fact, we put forward a proposal for the generation of variational plaquette PEPSs [89,91] while speculating on potential implementation of 2D TN states in scalable ion-trap architectures that allow ion-crystal reconfiguration.

In Appendix E, we discuss a detailed schedule of operations for a 5×5 lattice in a well-tested microstructured ion trap [102]. Ultimately, we are confident that scalable realization of the TN circuit for 2D systems in simpler trap architectures can be achieved by implementing in-sequence projective measurements and reset of individual ions [93]. Indeed, assessing the optimal implementation scheme for a given trap architecture will be the focus of future research.

The demonstrated experimental capabilities open opportunities for ion-trap implementation of a variety of protocols that make use of 1D variational tensor-network circuits. These include protocols to study infinite 1D systems [47,48], imaginary- and real-time evolution [106], and quantum machine learning [107]. Finally, the resonant interactions with one or several phonon modes potentially can be used to construct circuits beyond the TN *Ansätze*, e.g., to address problems in quantum chemistry [50,108]. The design of the appropriate variational circuit might be obtained in a closed-loop optimization on a quantum device itself using recent hybrid algorithms such as adaptive algorithm [109] or reinforcement learning [110].

ACKNOWLEDGMENTS

We gratefully acknowledge funding by the Austrian Research Promotion Agency Contracts No. 872766 (project AutomatiQ) and No. 884471 (project ELQO), and No. 877616 (project ALFQC), the Austrian Science Fund via the SFB BeyondC project No. F7109, the EU via QuantERA project T-NiSQ, the ERC Starting Grant QCosmo Grant No. 948893, and the U.S. Air Force Office of Scientific Research IOE Grant No. FA9550-19-1-7044 (project LASCEM). We further receive support from the European Union's Horizon 2020 research and innovation program under the Marie Skłodowska-Curie Grant Agreement No. 840450 and from the IQI GMBH. Our work reflects only the views of its authors, all agencies are not responsible for any use that may be the direct or indirect result of the information contained in this paper.

M. M. and V. K. contributed equally to this work.

APPENDIX A: COMPARISON OF ION-TRAP RESOURCES FOR TN VQE

In our work, we exploit monochromatic single-qubit operations exciting the motional sideband as the elementary resource. We now compare our approach to off-resonant bichromatic operations as proposed by Mølmer and Sørensen [54,111], which can be implemented either adiabatically or nonadiabatically [112,113]. Both techniques operate on different timescales; the adiabatic MS gate is a second-order perturbative process and scales quadratically in the Lamb-Dicke parameter η, which is small in the Lamb-Dicke regime $\eta \ll 1$ [114]. In contrast, the nonadiabatic MS gate disentangles the qubits from the motion at characteristic times $\tau = \pi/\eta\Omega$, making it effectively linear in η. Consequently, the nonadiabatic approach is about an order of magnitude faster than the adiabatic gate and can be realized in a few tenths of microseconds.

Assuming a simple two-level model of the atom, tuning the rotation angles of the nonadiabatic MS gate requires only a fixed ratio between the gate duration τ and the detuning of the laser field from the motional sideband. In practice, additional levels of the atom will introduce additional ac Stark shifts, which need to be compensated for high-fidelity gate operations [115,116]. While strategies allowing for continuous gate parameters with MS gates do exist [113], in our setup, experience shows that it is not possible to characterize and predict these shifts with sufficient accuracy to not limit the performance. Additionally, addressing pairs of qubits comes at the cost of next-neighbor crosstalk, which further impacts the system by introducing correlated errors, which spread uncontrollably. For these reasons, the blue-sideband operations are—at least in our experimental apparatus—better suited for VQEs.

We thus analyze the TN VQE with our BSB operations as resources compared to alternative circuits using MS gates with precalibrated (fixed) angles and single-qubit Z rotations. Two scenarios are considered: (i) n-qubit MS gates acting locally on all n qubits in each variational block as shown in Fig. 7(a) and (ii) local two-qubit MS gates acting on nearest neighbors in Fig. 7(b). Our target is the eight-qubit SSH model at $\delta = 0$ and $t_- = 0.5$. It was already shown in Ref. [46] that parametrized MS operations and local σ^z rotations can be used to target this model. As we mention above, fast nonadiabatic MS gates are typically calibrated for certain angles and cannot be used as a resource in variational circuits; therefore, the tunable parameters are the angles of the σ^z rotations.

We compare the infidelity of the prepared states with the true ground state of the SSH model versus the number of variational parameters in the circuit in Fig. 7(c). Similar to the main text of this manuscript, we fix the size of the variational boxes to two on the edges and to three in the bulk. The circuit using sideband operations is similar to the one presented in this manuscript. In the circuits using MS operations, for each number of variational parameters, we choose a fixed angle of all MS gates among a set of values $\{\pi/16, \pi/8, \pi/4\}$ to mimic the experiment. Each circuit is reoptimized for multiple initial parameter sets. For the circuits using sideband pulses, we consider two initial states of the phonon mode: (i) a perfectly cooled state with the average number of phonons $n = 0$ and (ii) a state with finite temperature $n = 0.01$. The circuits using MS operations are considered without imperfections.

The data presented in Fig. 7(c) demonstrate that the variational circuit using sideband resources can perform better than the alternative circuits for the same number of variational parameters. Moreover, for a realistic initial temperature of the phonon mode, the performance of the

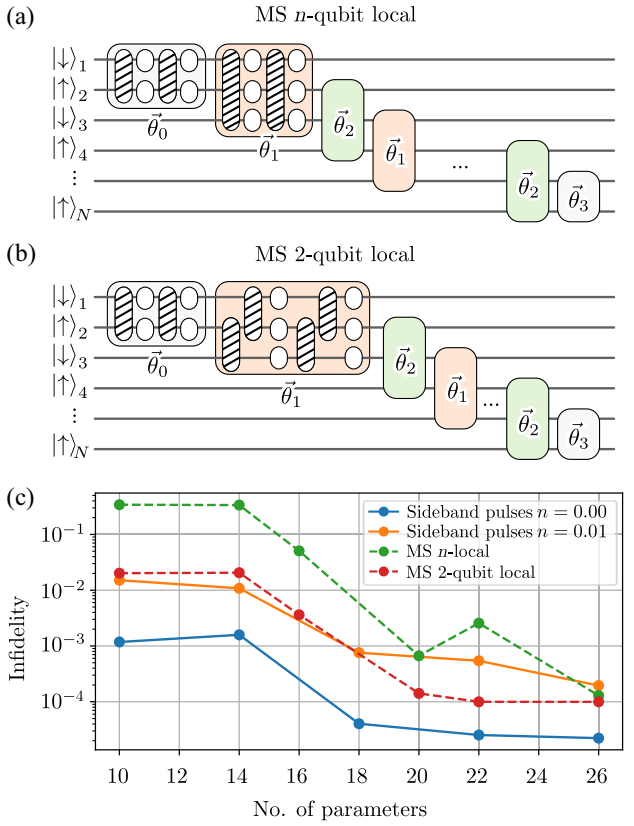

FIG. 7. Efficiency comparison for the variational *Ansatz* circuits: circuit using the sideband operations considered in the present paper with $n = 0$ and $n = 0.01$ average number of phonons in the initial thermal state of the c.m. mode and the alternative circuits (a) and (b) using the nonadiabatic MS operations with the fixed values and without experimental imperfections. In (a), MS operations can be applied to n local qubits and, in (b), only to neighbor pairs of qubits. The MS operations (with the optimal fixed angle) are given by pattern-filled ovals. White ovals represent variational σ_i^z rotations. (c) Optimized infidelity for the eight-qubit SSH model at $\delta = 0$, $t_- = 0.5$ of the states prepared using the circuit for a given number of variational parameters.

sideband circuit remains comparable to the circuit using MS operations without additional experimental errors. In any implementation, these experimental errors will determine the achievable infidelity. We note that a quantitative comparison of these two approaches requires a detailed numerical analysis that depends crucially on the specific experimental parameters of the implementation. Thus, we resort to a qualitative discussion of the expected main error sources informed by our present experimental system:

(i) In our system, one of the main error sources is crosstalk due to optical imperfections in qubit addressing. Encoding the qubit in different, well-separated transitions as described in Sec. IV effectively suppresses unwanted coupling with immediate neighbors. However, this encoding scheme is applicable only for single-qubit gates: MS gates require the simultaneously addressed qubits to occupy the same subspace and as such, next-neighbor crosstalk will negatively impact the circuit.

(ii) The MS gate approach is inherently resilient to a nonzero initial phonon number of the QDB [99]. The blue-sideband approach requires more pulses and parameters to compensate for a nonzero initial phonon number. Both approaches are susceptible to heating of the phonon mode during a gate operation.

(iii) We expect that the effect of qubit decoherence is given by the length of the circuit for both approaches.

It should be noted that the experimental performance of a given approach depends crucially on the specific experimental parameters and requires a detailed error analysis using numerical simulations. In our system, crosstalk is the dominating error, and thus, we choose the blue-sideband approach.

APPENDIX B: ANALYSIS OF EXPERIMENTAL IMPERFECTIONS

In this section, we examine and compare different error models to explain the deviation between the experimental data and the predicted values for $\tilde{Z}_{R/T}$ in Figs. 2, 5, and 6 of the main text. We numerically simulate the variational circuit for $\delta = 4$ with the experimentally obtained optimal parameter sets $\boldsymbol{\theta}_{\text{opt}}$ considering the full circuit as a sequence of operations on the blue sideband; errors are modeled to occur after each individual sideband operation. We quantify the performance of the considered error models via the residual sum of squares (RSS)

$$\text{RSS} = \sum_i (\tilde{Z}_i^{\text{data}} - \tilde{Z}_i^{\text{model}})^2$$

with i labeling each point obtained for $\tilde{Z}_{R/T}$. From the following analysis, we conclude that, in our task, the initial temperature of the c.m. mode can significantly affect only the symmetry-broken phase. Because of the finite temperature, the VQE can prepare a low-energy symmetry-broken state instead of the symmetric exact ground state. However, this imperfection is not relevant for investigating condensed matter phases. We identify the dominant sources of errors as the c.m. mode heating, fluctuations of the tip voltages of the trap electrodes, and imperfect compensation of the Stark shift, which effectively result in depolarization of the prepared states along the quantization axis of the qubits.

1. Finite temperature of the c.m. mode

We investigate the effect of finite temperature of the c.m. mode in the initial state caused by imperfect cooling. In Fig. 8, we show the results of the numerical simulation of the VQE where we consider the mean phonon numbers $\bar{n} = 0.00$ and $\bar{n} = 0.05$ in the thermal state of the c.m. mode. Here we do not include heating and dephasing, as these mechanisms are considered individually in the next

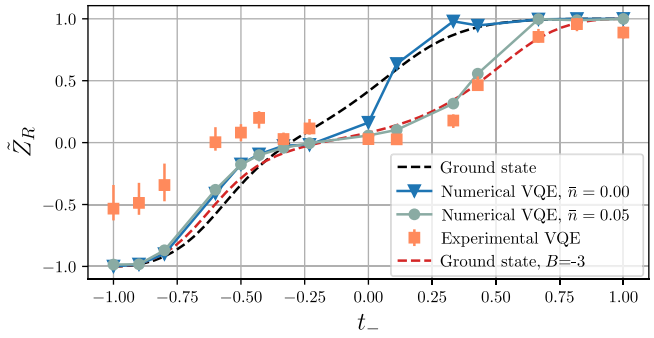

FIG. 8. Partial reflection MBTI $\tilde{Z}_R$, Eq. (7), for the extended SSH model, Eq. (B1), at $\delta = 4$ with $N = 8$ and $n = 4$. The dashed lines give the MBTIs from the exact ground states. In black we show the ground state without a pinned magnetic field $B = 0$, while red depicts the case with $B = -3$; see the text. Numerical simulations of the VQE with the c.m. mode having a mean phonon number $\bar{n} = 0$ and $\bar{n} = 0.05$ are shown by the solid lines. The experimentally measured data are represented by squares.

section. For both values of $\bar{n}$, we observe no shift of $\tilde{Z}_R$ in the topological phase, which, in contrast, is present in our experimental data. However, in the symmetry-broken phase, unlike for $\bar{n} = 0$, the case for $\bar{n} = 0.05$ demonstrates results close to the experimentally obtained values. For $\bar{n} = 0.05$, we obtain a residual sum of squares RSS $= 1.11(96)$ for $\tilde{Z}_R$ and RSS $= 1.92(48)$ for Z_T; when averaged, we get RSS $= 1.52(22)$. In contrast, $\bar{n} = 0.00$ yields larger deviations, namely, RSS $= 2.41(76)$ for $\tilde{Z}_R$ and RSS $= 3.23(46)$ for Z_T [averaged RSS $= 2.82(61)$].

We attribute the significant difference in the MBTIs for the cases $\bar{n} = 0.00$ and $\bar{n} = 0.05$ in the symmetry-broken phase to the ground-state degeneracy. At finite size, the exact model resolves this degeneracy. In the unique finite-size ground state, the parity symmetry is not spontaneously broken, as shown in the top left panel of Fig. 9, which gives the reduced states of four middle qubits in the ground state of the ESSH model at $\delta = 4$ and $t_- = 0.333$. In contrast, due to the finite temperature of the c.m. mode, the VQE algorithm polarizes into a physical ground state with spontaneous symmetry breaking as indicated by the top right panel in Fig. 9. This state is less entangled, has smaller finite-size effects, and is thus closer to the value $\tilde{Z}_R = 0$ in the thermodynamic limit.

The fragility of the global energy minimum corresponding to the exact ground state of the ESSH model at $\delta = 4$, $t_- = 0.333$ is shown in Fig. 8. We simulate the variational circuit for a range of parameters $\boldsymbol{\theta}(\alpha) = (1-\alpha)\boldsymbol{\theta}_{\text{opt}}|_{\bar{n}=0} + \alpha\boldsymbol{\theta}_{\text{opt}}|_{\bar{n}=0.05}$, which interpolates between the optimal parameters $\boldsymbol{\theta}_{\text{opt}}|_{\bar{n}=0}$ found by the VQE for the cases with $\bar{n} = 0$ and the optimal parameters $\boldsymbol{\theta}_{\text{opt}}|_{\bar{n}=0.05}$ found for $\bar{n} = 0.05$. For the respective states, we calculate the relative energy error $\Delta_{\text{rel}} = [E_{\text{targ}} - E(\boldsymbol{\theta})]/E_{\text{targ}}$ with respect to the ground-state energy and compute the corresponding values of $\tilde{Z}_R$.

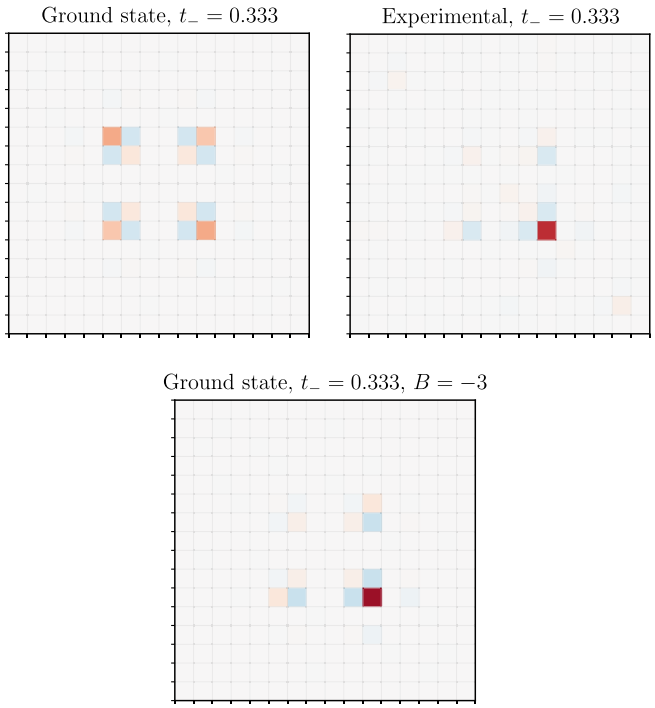

FIG. 9. Reduced density matrices of the four central ions in an eight-ion system. The top left state corresponds to the ground state at $t_- = 0.333$. The experimentally measured data for same t_- are shown in the right top state. In the bottom panel, we show the ground state of the ESSH model with a pinned magnetic field $B = -3$ [see Eq. 12] for $t_- = 0.333$, which is in good agreement with the experimental data.

At $\alpha = 0$ and $\alpha = 1$, Δ_{rel} exhibits two local minima as shown in Fig. 10. For $\bar{n} = 0$, the global minimum corresponds to the symmetric state at $\alpha = 0$, while at $\bar{n} = 0.05$ we observe a substantial energy shift. In contrast, the symmetry-broken state at $\alpha = 1$ demonstrates almost no energy shift when $\bar{n}$ increases; thus, its energy becomes the

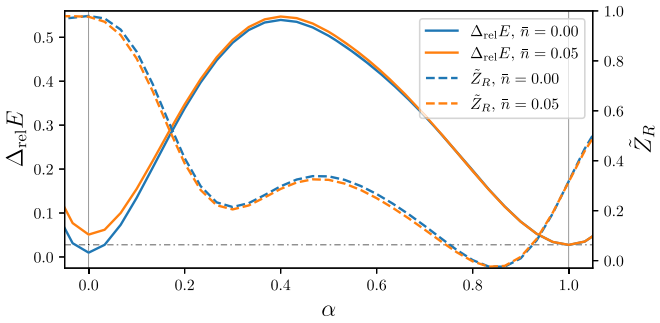

FIG. 10. Numerical simulation of the *Ansatz* circuit in Fig. 1 for a range of parameter sets $\boldsymbol{\theta}(\alpha)$ parametrized by α (see the text) for the mean phonon numbers $\bar{n} = 0$ and $\bar{n} = 0.05$. The left vertical axis gives the relative energy error of the obtained states with respect to the exact ground-state energy of the ESSH model at $\delta = 4$, $t_- = 0.333$; the right axis gives the corresponding value of partial-reflection MBTI $\tilde{Z}_R$.

global minimum for $\bar{n} = 0.05$. This robustness is a result of the smaller amount of entanglement in the reduced bulk state compared to the exact ground state—this is highlighted by the top panels in Fig. 9.

Breaking of the symmetry can also be achieved in the target ESSH model by introducing sufficiently large pinned staggered magnetic field B on the outermost ions

$$H_{\mathrm{ESSH}} = \sum_{k=1}^{N-1}[1 + (-1)^{k-1}t_-] \times (\sigma_k^x\sigma_{k+1}^x + \sigma_k^y\sigma_{k+1}^y + \delta\sigma_k^z\sigma_{k+1}^z) + B(\sigma_1^z - \sigma_N^z). \tag{B1}$$

For $B = -3$, the exact ground state is in good agreement with the experimental data, as shown in Fig. 8 by the red dashed line. This is also evident from the density matrices in Fig. 9 when directly comparing the top right and bottom panels. With increasing system size, the gap between the ground state and the first excited states decreases, in turn also decreasing the required pinning field B until it vanishes in the thermodynamic limit.

Our analysis shows that for fixed circuit parameters $\boldsymbol{\theta}$, moderate temperature of the initial state of the c.m. mode does not affect the MBTIs significantly. Instead, it can cause the VQE to obtain different optimal parameters $\boldsymbol{\theta}_{\mathrm{opt}}$, preparing a physical low-energy state with broken symmetry instead of the exact symmetric ground state in the symmetry-broken phase. This imperfection, however, is not important when investigating phases of quantum matter, since, in the thermodynamic limit, the same symmetry breaking occurs spontaneously regardless.

2. Heating of motional modes

Residual noise, most importantly due to electric field fluctuations in the ion trap, disturbs the motional state of the ion string, causing the string to heat up. In our setup, these perturbations occur at a rate $\Gamma_H = 27(1)$ phonons per second. This effect is modeled by the channel

$$\rho \to \rho' = (1 - p)\cdot\rho + p\cdot\hat{a}^\dagger\varrho\hat{a}$$

inducing an error with probability $p = t\Gamma_H$ on the state ρ depending on the time $t \ll 1/\Gamma_H$. We simulate heating in the circuits with the initial states having different temperatures, namely, $\bar{n} = 0.00$ and $\bar{n} = 0.05$. To establish a notion of time, we assume each blue-sideband operation implementing $|S, n = 0\rangle \to |D, n = 1\rangle$ to require a laser pulse of length $t_\pi = 125$ μs. In Figs. 11(a) and 11(b), we observe a significant effect on the MBTIs $\tilde{Z}_{R/T}$ in the topological phase $t_- \to -1$, which is less pronounced in the trivial phase $t_- \to +1$. However, we see deviations in $\tilde{Z}_T$, which tend to increase as we approach $t_- = 1$. These can be attributed to different lengths T required to execute the pulse sequences as shown in Fig. 12. As T grows when approaching the edge cases $t_- \to \pm 1$, these sequences are more affected by heating effects. Considering a perfectly cooled initial state with a mean phonon number $\bar{n} = 0$, the residual sum of squares is given by $\mathrm{RSS} = 0.84(21)$ for $\tilde{Z}_R$ and $\mathrm{RSS} = 0.45(11)$ for $\tilde{Z}_T$; when averaged, we obtain $\mathrm{RSS} = 0.65(16)$. Increasing the initial temperature to $\bar{n} = 0.05$ yields $\mathrm{RSS} = 0.71(18)$ for $\tilde{Z}_R$ and $\mathrm{RSS} = 0.35(10)$ for Z_T [average $\mathrm{RSS} = 0.65(16)$]. However, as we discuss in the previous subsection, the temperature of the initial state does not affect the MBTIs significantly for fixed circuit parameters.

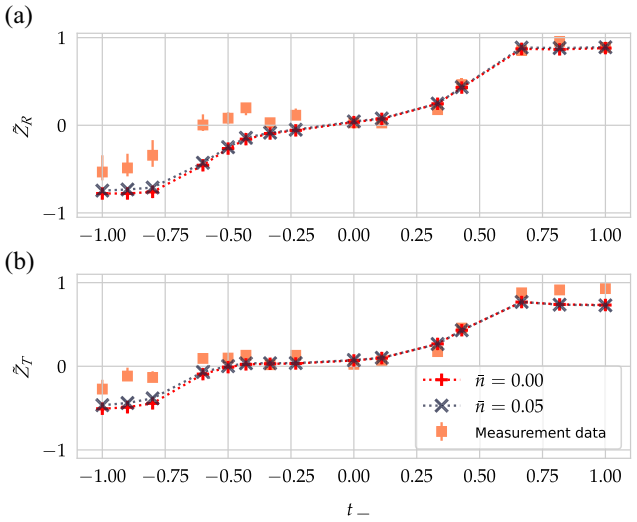

FIG. 11. Simulated heating of the motional modes for mean phonon numbers $\bar{n} = 0.00$ and $\bar{n} = 0.05$ of the initial state. The time reference is established via the average laser-pulse length $t_\pi = 125$ μs required to implement a π flip on the blue sideband.

3. Depolariziation and weighted Pauli errors

Decoherence processes on the motional modes translate into errors on the addressed qubits. Such errors can be modeled by a depolarizing channel, where each spatial axis is equally affected by a product of single-qubit Pauli errors $\sigma_i^{(x,y,z)}$ with probability $p/3$. In reality, it is unlikely that all errors are distributed equally; thus, we must consider

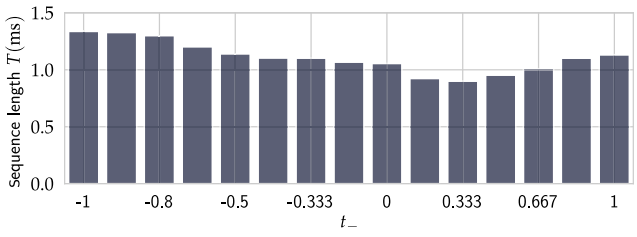

FIG. 12. Lengths T of the individual laser-pulse sequences required to implement the desired target state. T increases as t_- approaches ± 1, giving the system more time to be affected by heating.

probabilities for each axis p_x, p_y, and p_z, such that for a system of N qubits

$$\rho' = (1 - \sum_{j\in\{x,y,z\}} p_j)^N \rho + \prod_i^N \sum_{j\in\{x,y,z\}} p_j \hat{\sigma}_i^j.$$

For simplicity, we assume $p_x = p_y = p_{xy}$, which is shown to be valid in simulations, where exchanging p_x for p_y and vice versa yields identical results. We evaluate the model for both $\tilde{Z}_R$ and $\tilde{Z}_T$ for all combinations $p_{xy,z} = \{0, 0.001, 0.005, 0.01, 0.02, 0.03, 0.04\}$ and estimate the "goodness of fit" via the RSS to deduce the most likely source of error in our setup. Note that this analysis also considers the case without any errors, i.e., $p_{xy} = p_z = 0$.

The results of our comparison are shown in Figs. 13(a) and 13(b). The best fit is achieved when $p_{xy} = 0$ and $p_z = 0.03$ for both MBTIs. We obtain a RSS $= 0.17(7)$ for $\tilde{Z}_R$ and RSS $= 0.098(35)$ in $\tilde{Z}_T$ [RSS $= 0.13(5)$ when averaged] and conclude that the circuit is predominantly impacted by dephasing, resulting in Z-type errors. From a purely experimental point of view, this argument is expected for two reasons: First, even in the presence of laser intensity and laser phase noise, we are able to control the rotation angles θ and ϕ of single-qubit gates to an extent such that we can achieve average gate fidelities of beyond 99.99%. Second, the VQE algorithm is supposed to take systematic over- and under-rotations into account when converging to an optimal set of circuit parameters $\boldsymbol{\theta}_{\text{opt}}$. The observed Z errors are a consequence of various sources: We expect contributions due to heating and dephasing of the motional states as well as residual detuning from the first blue sideband, which is a consequence of imperfect Stark shift compensation.

We also consider a finite temperature of the initial state with mean phonon number of $\bar{n} = 0.05$ and evaluate the model's performance. The results are shown in Fig. 14. We find a best fit for the probabilities $p_{xy} = 0$ and $p_z = 0.03$ in agreement with the data obtained for the ideally cooled initial state. The residual sum of squares is RSS $= 0.15(7)$ for $\tilde{Z}_R$ and RSS $= 0.081(32)$ for $\tilde{Z}_T$. When averaged, we find an overall RSS $= 0.12(5)$. This analysis yields a better agreement than the previous analysis for $\bar{n} = 0.00$; however, we find the RSS to overlap within their margin of errors.

4. Comparison of error models

To conclude this section, we compare the individual models via their respective RSSs in Table I: heating of the phonon mode with a rate $\Gamma_H = 27(1)$ phonons per second and a model considering dephasing of the qubits with $p_z = 0.03$, neglecting X and Y errors. We consider both cases of a perfectly cooled initial state $\bar{n} = 0.00$ and a finite-temperature state $\bar{n} = 0.05$. As it is evident from both models, the initial temperature in the considered range has only a small effect. For $\bar{n} = 0.05$, we find an average

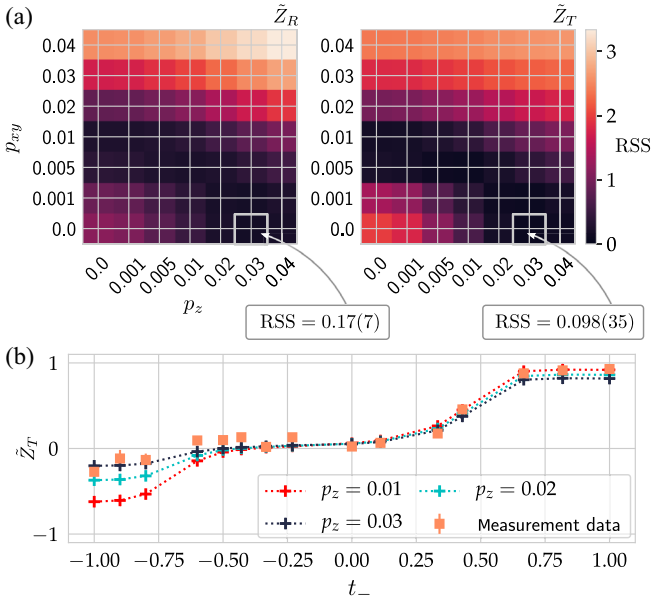

FIG. 13. Goodness-of-fit estimation via residual sum of squares for the weighted Pauli error model. We compare the model with the data for $\tilde{Z}_R$ and $\tilde{Z}_T$ individually in (a). As we expect X and Y errors to occur with the same probability, we assume $p_x = p_y = p_{xy}$. The best fit is achieved for $p_{xy} = 0$ and $p_z = 0.03$ with RSS $= 0.17(7)$ in $\tilde{Z}_R$ and RSS $= 0.098(35)$ in $\tilde{Z}_T$ shown in (b), respectively.

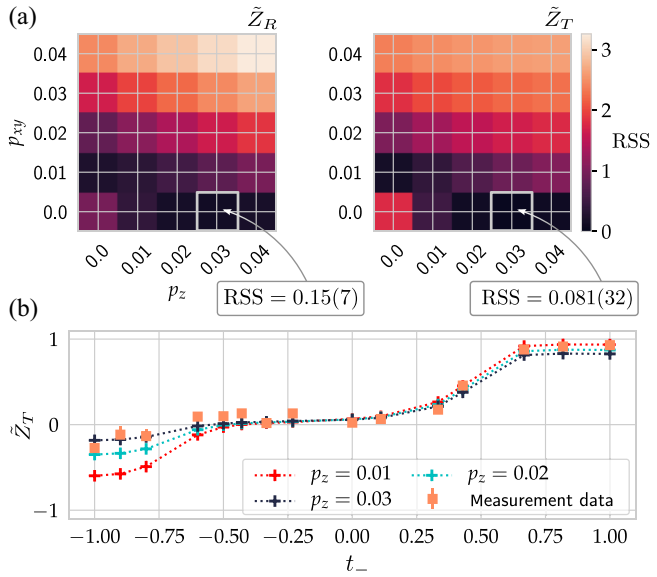

FIG. 14. (a) Residual sum of squares of the weighted Pauli error model for the MBTIs $\tilde{Z}_R/T$ considering an imperfectly cooled initial state with mean phonon number $\bar{n} = 0.05$ for different probabilities $p_{xy,z}$. We obtain a RSS $= 0.15(7)$ in $\tilde{Z}_R$ and RSS $= 0.081(32)$ [average RSS $= 0.12(5)$] shown in (b) for $\tilde{Z}_T$.

TABLE I. Comparison of the RSS obtained for the "best fit" of the considered error models. We show the values obtained for $\tilde{Z}_R$ and $\tilde{Z}_T$ as well as their average for different mean phonon numbers $\bar{n}$ of the initial state.

Model	$\bar{n}$	RSS $\tilde{Z}_R$	RSS $\tilde{Z}_T$	RSS (av)
Finite temperature	0.00	2.41(76)	3.23(46)	2.82(61)
	0.05	1.11(96)	1.92(48)	1.52(22)
Heating	0.00	0.84(21)	0.45(11)	0.65(16)
	0.05	0.71(18)	0.35(10)	0.53(14)
Pauli $p_z = 0.03$	0.00	0.17(7)	0.098(35)	0.13(5)
	0.05	0.15(7)	0.081(32)	0.12(5)

$\mathrm{RSS} = 0.53(14)$ assuming errors are related only to heating of the phonon mode, compared to $\mathrm{RSS} = 0.12(5)$ for the weighted Pauli model. Dephasing of the qubits is attributed to various mechanisms: First, heating yields to the occupation of different motional states, each evolving with a different frequency depending on the number of phonons. Second, fluctuations of the tip voltages of the trap electrodes induce phases on the c.m. mode, in turn inducing a phase shift on the qubits upon each sideband operation. A third mechanism is imperfect compensation of the Stark shift resulting in a small detuning from the first blue sideband of the c.m. mode. All of these sources manifest as Z errors. As increasing the system size N extends the length of the circuit while simultaneously decreasing the coherence time of the c.m. mode, these errors will become evermore relevant when adding more qubits. In contrast, systematic X and Y errors do not impact the measurement outcomes, as the VQE tunes the rotation angles to implement the desired operations.

APPENDIX C: A FOUR-QUBIT SSH TEST BED

We test our blue-sideband sequences on the smallest instance of the SSH model, namely, on a system of four qubits. The circuit follows the scheme shown in Fig. 1(a). However, the final "box" $\boldsymbol{\theta}_D$ is executed right after $\boldsymbol{\theta}_C$ on qubits 3 and 4. We obtain the optimal parameter set $\boldsymbol{\theta}_{\mathrm{opt}}$ from theory; the 14 angles (in units of π) required to implement the circuit are given in Table II.

TABLE II. Rotation angles for the individual boxes of the circuit shown in Fig. 1(a) for the four-qubit test-bed system; all angles are given in units of π.

Box	Angles (π)				
$\boldsymbol{\theta}_A$	1.2036	−0.3984			
$\boldsymbol{\theta}_B$	0.1526	0.9366	−1.1738	0.067	−0.0562
$\boldsymbol{\theta}_C$	−0.9232	1.5904	−0.1288	−1.0344	−2.8254
$\boldsymbol{\theta}_D$	0.1792	3.8938			

APPENDIX D: BULK TOMOGRAPHY AND FRAGILITY OF THE MBTIs

As an additional quality estimator for the ground-state preparation, we also carry out the full quantum-state tomography restricted to the bulk sites (i.e., the four central ion qubits in the chain). Here, we reconstruct the experimental four-site density matrices from projective measurements in all possible combinations of Pauli bases. Similarly, we acquire the reduced density matrix from exact numerical simulations of the TN VQE circuit using the pulses optimized on the experiment (but omitting error channels). Then, we compare both of these density matrices with the true ground state calculated via exact diagonalization and estimate the quality of the ground-state preparation (for the bulk sites) by calculating the mixed-state fidelity.

Such an analysis is carried out for the case $\delta = 0$, where the ground state is always nondegenerate in the bulk, and thus bulk-state fidelity is a good quality indicator. Our study shows that even for the experimental data, which are exposed to real noise, we are always capable of achieving a bulk fidelity well above 80% (and mostly close to 90%), corroborating the success of our strategy toward ground-state preparation, with remarkably high quality as shown in Fig. 15. As a point of interest, we observe that the loss of fidelity in states of the topological phase ($t \approx -1$) is small compared to the deviation of the MBTI from the theoretical value that we observe, e.g., in Fig. 5. This is especially pronounced for the time-reversal MBTI $\tilde{Z}_T$. The larger deviation is attributed to the fact that the MBTI is not the expectation value of an observable (i.e., it is not a linear functional of the density matrix), and thus, its error is not bound linearly by the infidelity. In this sense, this analysis seems to suggest to us that the MBTIs $\tilde{Z}_{R/T}$ are fragile phase indicators under experimental noise, since the measured errors are large even when the ground-state preparation is rather accurate.

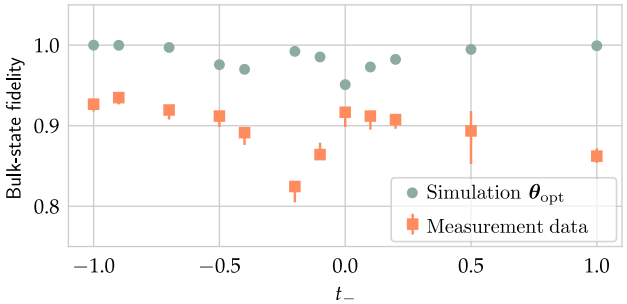

FIG. 15. Fidelity of the variationally implemented state in the bulk obtained by state tomography on the bulk qubits. A simulation of the state using the optimal parameters $\boldsymbol{\theta}_{\mathrm{opt}}$ is shown for direct comparison. Experimentally, we achieve a fidelity of >80% over the whole parameter regime for the case $\delta = 0$.

APPENDIX E: PROPOSED IMPLEMENTATION OF A 2D TN VQE IN A NOVEL ION TRAP

In this section, we speculate on a potential preparation of plaquette PEPS [91] with 2D TN VQE using a novel quantum technology of a linear ion trap as quantum hardware [102]. We demonstrate a minimal scheme involving 25 ions, which can exploit bulk-translation invariance in the target state; the TN diagram is shown in Fig. 16(a). Similar to the MPS diagram in Fig. 1(c), the plaquettes encode a sequence of unitary operations on local sets of ions.

The architecture of choice is shown in Fig. 16(b) and has already been tested under experimental conditions [102]. It incorporates four "storage" branches, which are used to load and store ions. Via "shuttling" zones, the ions can be moved to the central "quantum region" (QR), where they reside in a common potential and thus share a (local) phonon mode. Similar to the scheme in Figs. 1(a) and 1(b), we use single-ion sideband operations to implement a variational unitary. However, we need to consider controlled reconfigurations of ion string(s) in the QR to realize the different plaquettes; these reconfigurations are implemented by modulation of individual trap electrodes. We employ three operations, namely, (1) shuttling operations, where ions are moved in between different trap zones, (2) "splits," which divide an ion string into substrings, and (3) "merges," where substrings are joined into one, larger string.

We now show how the TN in Fig. 16(a) can be mapped to the chosen trap architecture. Considering the lower left corner of the TN diagram, we sketch the ion string reconfiguration operations required to realize the first three plaquettes A, B, and C in detail in Fig. 16(c); optical single-qubit sideband operations are not explicitly shown. The ions are represented by colored circles, where empty gray circuits are considered "fresh" resources, i.e., ions that have not yet participated in the circuit. Solid gray circles indicate ions that have already been addressed but must be kept in one of the memory regions to be used in later plaquettes. Finally, solid black circles show those ions that have already "dropped out" of the circuit; they are thus parked in the lower left branch of the trap. To better identify the movement of individual ions, we assign tuples of integers (n, m), which correspond to the column and row of the particle in the TN diagram.

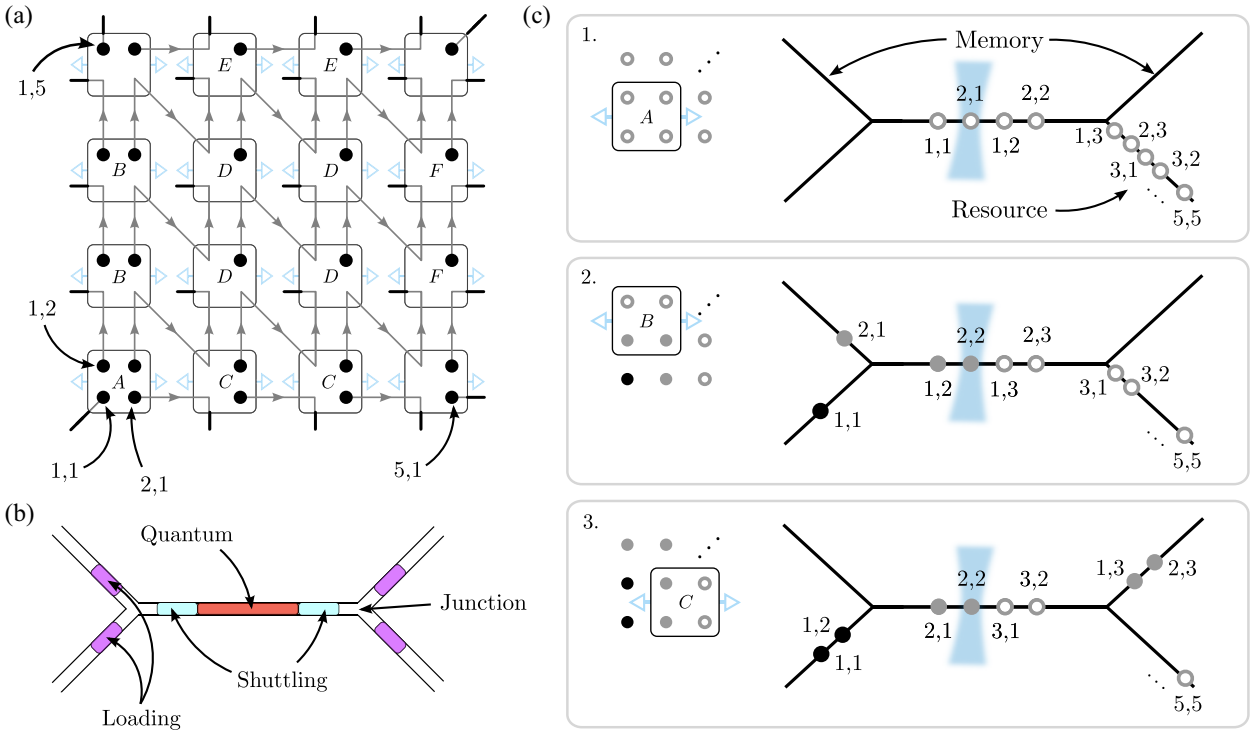

FIG. 16. Tensor-network VQE in a possible architecture of a 2D ion trap. (a) TN representation of a 2D circuit in a system of 5×5 ions (circles). Each plaquette couples four qubits to a local phonon mode via sideband operations similar to Fig. 1. Plaquettes labeled by identical letters can share variational parameters to enforce the approximate translational invariance. (b) A suitable linear trap architecture [102]. The quantum region in the center is connected to four branches, which serve as loading and memory zones. Ions can be shuttled in between regions by precise control of local trap potentials. (c) Possible implementation of the 2D circuit via sideband and shuttling operations. We show the first three steps in the circuit with all participating ions shuttled to their respective positions. Here, empty gray circles indicate ions that have thus far not participated in the circuit, while those in solid gray have already been addressed and must be kept for later use in different plaquettes. Black circles highlight ions that have already dropped out of the circuit and remain from this point on untouched.

TABLE III. Required number of shuttling, split, and merge operations to realize each of the first three plaquettes of the TN diagram for the given trap configuration; see Fig. 16.

Step	Shuttling	Split	Merge	Total
1	1	1	0	2
2	3	4	1	7
3	4	3	2	7

(1) We implement the first plaquette A by shuttling four ions from the resource register to the QR region. Note that the initial arrangement of the qubits is chosen such that the number of required reconfigurations required in later plaquettes are minimized.
(2) Continuing with B, we can move qubit (1,1) to the lower left branch. This ion will not participate in subsequent plaquettes. Ion (2,1) is split from the substring (1,2) and (2,2) and shuttled to the left memory. Two more ions (1,3) and (2,3) join the QR and merge with the aforementioned substring.
(3) Plaquette C requires more reordering: (1,3) and (2,3) are moved to the right memory, while (1,2) is parked next to (1,1). Ion (2,1) is shuttled back to the QR and joins (2,2) with two more ions (3,1) and (3,2) from the resource branch.

In total, we need to implement 15 reconfiguration operations to implement the first three plaquettes; the individual operations are listed in Table III. We extend our investigation to the full circuit, ending up with a total of 152 operations. However, the feasibility of such demanding circuits remains an open question. Recently, a fault-tolerant parity readout scheme has been realized, requiring more than 40 split-and-merge operations and 110 shuttlings including state preparation and readout [117]. However, the trap geometry used in this experiment does not feature branches as memory regions; an implementation in the trap architecture described in this section might greatly simplify the circuit.

[1] M. Z. Hasan and C. L. Kane, *Colloquium: Topological Insulators*, Rev. Mod. Phys. **82**, 3045 (2010).
[2] X. L. Qi and S. C. Zhang, *Topological Insulators and Superconductors*, Rev. Mod. Phys. **83**, 1057 (2011).
[3] K. J. Satzinger *et al.*, *Realizing Topologically Ordered States on a Quantum Processor*, Science **374**, 1237 (2021).
[4] G. Semeghini, H. Levine, A. Keesling, S. Ebadi, T. T. Wang, D. Bluvstein, R. Verresen, H. Pichler, M. Kalinowski, R. Samajdar, A. Omran, S. Sachdev, A. Vishwanath, M. Greiner, V. Vuletic, and M. D. Lukin, *Probing Topological Spin Liquids on a Programmable Quantum Simulator*, Science **374**, 1242 (2021).
[5] P. Sompet, S. Hirthe, D. Bourgund, T. Chalopin, J. Bibo, J. Koepsell, P. Bojović, R. Verresen, F. Pollmann, G. Salomon, C. Gross, T. A. Hilker, and I. Bloch, *Realising the Symmetry-Protected Haldane Phase in Fermi-Hubbard Ladders*, Nature (London) **606**, 484 (2022).
[6] X.-G. Wen, *Choreographed Entanglement Dances: Topological States of Quantum Matter*, Science **363**, eaal3099 (2019).
[7] I. Affleck, T. Kennedy, E. H. Lieb, and H. Tasaki, *Rigorous Results on Valence-Bond Ground States in Antiferromagnets*, Phys. Rev. Lett. **59**, 799 (1987).
[8] A. Kitaev, *Fault-Tolerant Quantum Computation by Anyons*, Ann. Phys. (Amsterdam) **303**, 2 (2003).
[9] S. Bravyi, B. Leemhuis, and B. M. Terhal, *Topological Order in an Exactly Solvable 3D Spin Model*, Ann. Phys. (Amsterdam) **326**, 839 (2011).
[10] D. Perez-Garcia, F. Verstraete, M. M. Wolf, and J. I. Cirac, *Matrix Product State Representations*, Quantum Inf. Comput. **7**, 401 (2007), https://dl.acm.org/doi/10.5555/2011832.2011833.
[11] U. Schollwöck, *The Density-Matrix Renormalization Group in the Age of Matrix Product States*, Ann. Phys. (Amsterdam) **326**, 96 (2011).
[12] R. Orús, *A Practical Introduction to Tensor Networks: Matrix Product States and Projected Entangled Pair States*, Ann. Phys. (Amsterdam) **349**, 117 (2014).
[13] N. Schuch, M. M. Wolf, F. Verstraete, and J. I. Cirac, *Entropy Scaling and Simulability by Matrix Product States*, Phys. Rev. Lett. **100**, 030504 (2008).
[14] J. Eisert, M. Cramer, and M. B. Plenio, *Colloquium: Area Laws for the Entanglement Entropy*, Rev. Mod. Phys. **82**, 277 (2010).
[15] Y. Ge and J. Eisert, *Area Laws and Efficient Descriptions of Quantum Many-Body States*, New J. Phys. **18**, 083026 (2016).
[16] M. Aguado, J. I. Cirac, and G. Vidal, *Topology in Quantum States. PEPS Formalism and Beyond*, J. Phys. Conf. Ser. **87**, 012003 (2007).
[17] J. E. Moore, *The Birth of Topological Insulators*, Nature (London) **464**, 194 (2010).
[18] M. Levin and C. P. Nave, *Tensor Renormalization Group Approach to Two-Dimensional Classical Lattice Models*, Phys. Rev. Lett. **99**, 120601 (2007).
[19] R. Orús, *Exploring Corner Transfer Matrices and Corner Tensors for the Classical Simulation of Quantum Lattice Systems*, Phys. Rev. B **85**, 205117 (2012).
[20] I. M. Georgescu, S. Ashhab, and F. Nori, *Quantum Simulation*, Rev. Mod. Phys. **86**, 153 (2014).
[21] *National Academies of Sciences and Medicine*, *Manipulating Quantum Systems: An Assessment of Atomic, Molecular, and Optical Physics in the United States* (The National Academies Press, Washington, DC, 2020).
[22] E. Altman *et al.*, *Quantum Simulators: Architectures and Opportunities*, PRX Quantum **2**, 017003 (2021).
[23] S. Ebadi, T. T. Wang, H. Levine, A. Keesling, G. Semeghini, A. Omran, D. Bluvstein, R. Samajdar, H. Pichler, W. W. Ho *et al.*, *Quantum Phases of Matter on a 256-Atom Programmable Quantum Simulator*, Nature (London) **595**, 227 (2021).
[24] P. Scholl, M. Schuler, H. J. Williams, A. A. Eberharter, D. Barredo, K.-N. Schymik, V. Lienhard, L.-P. Henry, T. C. Lang, T. Lahaye *et al.*, *Quantum Simulation of 2D*

Antiferromagnets with Hundreds of Rydberg Atoms, Nature (London) **595**, 233 (2021).

[25] F. Arute, K. Arya, R. Babbush, D. Bacon, J. C. Bardin, R. Barends, R. Biswas, S. Boixo, F. G. Brandao, D. A. Buell *et al.*, *Quantum Supremacy Using a Programmable Superconducting Processor*, Nature (London) **574**, 505 (2019).

[26] C. Kokail, C. Maier, R. van Bijnen, T. Brydges, M. K. Joshi, P. Jurcevic, C. A. Muschik, P. Silvi, R. Blatt, C. F. Roos, and P. Zoller, *Self-Verifying Variational Quantum Simulation of Lattice Models*, Nature (London) **569**, 355 (2019).

[27] A. Mazurenko, C. S. Chiu, G. Ji, M. F. Parsons, M. Kanász-Nagy, R. Schmidt, F. Grusdt, E. Demler, D. Greif, and M. Greiner, *A Cold-Atom Fermi-Hubbard Antiferromagnet*, Nature (London) **545**, 462 (2017).

[28] J. Koepsell, J. Vijayan, P. Sompet, F. Grusdt, T. A. Hilker, E. Demler, G. Salomon, I. Bloch, and C. Gross, *Imaging Magnetic Polarons in the Doped Fermi-Hubbard Model*, Nature (London) **572**, 358 (2019).

[29] H. Sun, B. Yang, H. Y. Wang, Z. Y. Zhou, G. X. Su, H. N. Dai, Z. S. Yuan, and J. W. Pan, *Realization of a Bosonic Antiferromagnet*, Nat. Phys. **17**, 990 (2021).

[30] J. Vijayan, P. Sompet, G. Salomon, J. Koepsell, S. Hirthe, A. Bohrdt, F. Grusdt, I. Bloch, and C. Gross, *Time-Resolved Observation of Spin-Charge Deconfinement in Fermionic Hubbard Chains*, Science **367**, 186 (2020).

[31] M. Holten, L. Bayha, K. Subramanian, C. Heintze, P. M. Preiss, and S. Jochim, *Observation of Pauli Crystals*, Phys. Rev. Lett. **126**, 020401 (2021).

[32] M. A. Nichols, L. W. Cheuk, M. Okan, T. R. Hartke, E. Mendez, T. Senthil, E. Khatami, H. Zhang, and M. W. Zwierlein, *Spin Transport in a Mott Insulator of Ultracold Fermions*, Science **363**, 383 (2019).

[33] P. T. Brown, D. Mitra, E. Guardado-Sanchez, R. Nourafkan, A. Reymbaut, C.-D. Hébert, S. Bergeron, A.-M. Tremblay, J. Kokalj, D. A. Huse *et al.*, *Bad Metallic Transport in a Cold Atom Fermi-Hubbard System*, Science **363**, 379 (2019).

[34] C. Monroe, W. C. Campbell, L.-M. Duan, Z.-X. Gong, A. V. Gorshkov, P. W. Hess, R. Islam, K. Kim, N. M. Linke, G. Pagano, P. Richerme, C. Senko, and N. Y. Yao, *Programmable Quantum Simulations of Spin Systems with Trapped Ions*, Rev. Mod. Phys. **93**, 025001 (2021).

[35] J. Preskill, *Quantum Computing in the NISQ Era and Beyond*, Quantum **2**, 79 (2018).

[36] E. Farhi, J. Goldstone, and S. Gutmann, *A Quantum Approximate Optimization Algorithm*, arXiv:1411.4028.

[37] A. Peruzzo, J. McClean, P. Shadbolt, M.-H. Yung, X.-Q. Zhou, P. J. Love, A. Aspuru-Guzik, and J. L. O'Brien, *A Variational Eigenvalue Solver on a Photonic Quantum Processor*, Nat. Commun. **5**, 4213 (2014).

[38] P. J. O'Malley *et al.*, *Scalable Quantum Simulation of Molecular Energies*, Phys. Rev. X **6**, 031007 (2016).

[39] J. R. McClean, J. Romero, R. Babbush, and A. Aspuru-Guzik, *The Theory of Variational Hybrid Quantum-Classical Algorithms*, New J. Phys. **18**, 023023 (2016).

[40] N. Moll, P. Barkoutsos, L. S. Bishop, J. M. Chow, A. Cross, D. J. Egger, S. Filipp, A. Fuhrer, J. M. Gambetta, M. Ganzhorn, A. Kandala, A. Mezzacapo, P. Müller, W. Riess, G. Salis, J. Smolin, I. Tavernelli, and K. Temme, *Quantum Optimization Using Variational Algorithms on Near-Term Quantum Devices*, Quantum Sci. Technol. **3**, 030503 (2018).

[41] K. Bharti, A. Cervera-Lierta, T. H. Kyaw, T. Haug, S. Alperin-Lea, A. Anand, M. Degroote, H. Heimonen, J. S. Kottmann, T. Menke, W.-K. Mok, S. Sim, L.-C. Kwek, and A. Aspuru-Guzik, *Noisy Intermediate-Scale Quantum (NISQ) Algorithms*, Rev. Mod. Phys. **94**, 015004 (2022).

[42] C. Schön, E. Solano, F. Verstraete, J. I. Cirac, and M. M. Wolf, *Sequential Generation of Entangled Multiqubit States*, Phys. Rev. Lett. **95**, 110503 (2005).

[43] M. C. Bañuls, D. Pérez-García, M. M. Wolf, F. Verstraete, and J. I. Cirac, *Sequentially Generated States for the Study of Two-Dimensional Systems*, Phys. Rev. A **77**, 052306 (2008).

[44] H. Pichler, S. Choi, P. Zoller, and M. D. Lukin, *Universal Photonic Quantum Computation via Time-Delayed Feedback*, Proc. Natl. Acad. Sci. U.S.A. **114**, 11362 (2017).

[45] A. Smith, B. Jobst, A. G. Green, and F. Pollmann, *Crossing a Topological Phase Transition with a Quantum Computer*, Phys. Rev. Res. **4**, L022020 (2022).

[46] V. V. Kuzmin and P. Silvi, *Variational Quantum State Preparation via Quantum Data Buses*, Quantum **4**, 290 (2020).

[47] F. Barratt, J. Dborin, M. Bal, V. Stojevic, F. Pollmann, and A. G. Green, *Parallel Quantum Simulation of Large Systems on Small NISQ Computers*, npj Quantum Inf. **7**, 79 (2021).

[48] M. Foss-Feig, S. Ragole, A. Potter, J. Dreiling, C. Figgatt, J. Gaebler, A. Hall, S. Moses, J. Pino, B. Spaun, B. Neyenhuis, and D. Hayes, *Entanglement from Tensor Networks on a Trapped-Ion Quantum Computer*, Phys. Rev. Lett. **128**, 150504 (2022).

[49] Z.-Y. Wei, D. Malz, A. González-Tudela, and J. I. Cirac, *Generation of Photonic Matrix Product States with Rydberg Atomic Arrays*, Phys. Rev. Res. **3**, 023021 (2021).

[50] C. Hempel, C. Maier, J. Romero, J. McClean, T. Monz, H. Shen, P. Jurcevic, B. P. Lanyon, P. Love, R. Babbush, A. Aspuru-Guzik, R. Blatt, and C. F. Roos, *Quantum Chemistry Calculations on a Trapped-Ion Quantum Simulator*, Phys. Rev. X **8**, 031022 (2018).

[51] D. Paulson, L. Dellantonio, J. F. Haase, A. Celi, A. Kan, A. Jena, C. Kokail, R. van Bijnen, K. Jansen, P. Zoller, and C. A. Muschik, *Simulating 2D Effects in Lattice Gauge Theories on a Quantum Computer*, PRX Quantum **2**, 030334 (2021).

[52] T. Brydges, A. Elben, P. Jurcevic, B. Vermersch, C. Maier, B. P. Lanyon, P. Zoller, R. Blatt, and C. F. Roos, *Probing Rényi Entanglement Entropy via Randomized Measurements*, Science **364**, 260 (2019).

[53] J. I. Cirac and P. Zoller, *Quantum Computations with Cold Trapped Ions*, Phys. Rev. Lett. **74**, 4091 (1995).

[54] K. Mølmer and A. Sørensen, *Multiparticle Entanglement of Hot Trapped Ions*, Phys. Rev. Lett. **82**, 1835 (1999).

[55] D. Porras and J. I. Cirac, *Effective Quantum Spin Systems with Trapped Ions*, Phys. Rev. Lett. **92**, 207901 (2004).

[56] W. P. Su, J. R. Schrieffer, and A. J. Heeger, *Solitons in Polyacetylene*, Phys. Rev. Lett. **42**, 1698 (1979).

[57] A. Elben, J. Yu, G. Zhu, M. Hafezi, F. Pollmann, P. Zoller, and B. Vermersch, *Many-Body Topological Invariants*

from Randomized Measurements in Synthetic Quantum Matter, Sci. Adv. **6**, eaaz3666 (2020).

[58] F. Verstraete and J. I. Cirac, *Matrix Product States Represent Ground States Faithfully*, Phys. Rev. B **73**, 094423 (2006).

[59] J. Haegeman, D. Pérez-García, I. Cirac, and N. Schuch, *Order Parameter for Symmetry-Protected Phases in One Dimension*, Phys. Rev. Lett. **109**, 050402 (2012).

[60] F. Pollmann and A. M. Turner, *Detection of Symmetry-Protected Topological Phases in One Dimension*, Phys. Rev. B **86**, 125441 (2012).

[61] Q. A. Turchette, C. S. Wood, B. E. King, C. J. Myatt, D. Leibfried, W. M. Itano, C. Monroe, and D. J. Wineland, *Deterministic Entanglement of Two Trapped Ions*, Phys. Rev. Lett. **81**, 3631 (1998).

[62] V. Schäfer, C. Ballance, K. Thirumalai, L. Stephenson, T. Ballance, A. Steane, and D. Lucas, *Fast Quantum Logic Gates with Trapped-Ion Qubits*, Nature (London) **555**, 75 (2018).

[63] J. D. Wong-Campos, S. A. Moses, K. G. Johnson, and C. Monroe, *Demonstration of Two-Atom Entanglement with Ultrafast Optical Pulses*, Phys. Rev. Lett. **119**, 230501 (2017).

[64] D. Leibfried, R. Blatt, C. Monroe, and D. Wineland, *Quantum Dynamics of Single Trapped Ions*, Rev. Mod. Phys. **75**, 281 (2003).

[65] D. James, *Quantum Dynamics of Cold Trapped Ions with Application to Quantum Computation*, Appl. Phys. B **66**, 181 (1998).

[66] F. Schmidt-Kaler, H. Häffner, M. Riebe, S. Gulde, G. P. T. Lancaster, T. Deuschle, C. Becher, C. F. Roos, J. Eschner, and R. Blatt, *Realization of the Cirac-Zoller Controlled-NOT Quantum Gate*, Nature (London) **422**, 408 (2003).

[67] F. Schmidt-Kaler, H. Häffner, S. Gulde, M. Riebe, G. Lancaster, T. Deuschle, C. Becher, W. Hänsel, J. Eschner, C. Roos *et al.*, *How to Realize a Universal Quantum Gate with Trapped Ions*, Appl. Phys. B **77**, 789 (2003).

[68] S. Rommer and S. Östlund, *Class of Ansatz Wave Functions for One-Dimensional Spin Systems and Their Relation to the Density Matrix Renormalization Group*, Phys. Rev. B **55**, 2164 (1997).

[69] J. Eisert, M. Cramer, and M. B. Plenio, *Colloquium: Area Laws for the Entanglement Entropy*, Rev. Mod. Phys. **82**, 277 (2010).

[70] W. P. Su, J. R. Schrieffer, and A. J. Heeger, *Solitons in Polyacetylene*, Phys. Rev. Lett. **42**, 1698 (1979).

[71] W. P. Su, J. R. Schrieffer, and A. J. Heeger, *Soliton Excitations in Polyacetylene*, Phys. Rev. B **22**, 2099 (1980).

[72] E. J. Meier, F. A. An, and B. Gadway, *Observation of the Topological Soliton State in the Su-Schrieffer-Heeger Model*, Nat. Commun. **7**, 13986 (2016).

[73] F. Pollmann, A. M. Turner, E. Berg, and M. Oshikawa, *Entanglement Spectrum of a Topological Phase in One Dimension*, Phys. Rev. B **81**, 064439 (2010).

[74] F. Pollmann, E. Berg, A. M. Turner, and M. Oshikawa, *Symmetry Protection of Topological Phases in One-Dimensional Quantum Spin Systems*, Phys. Rev. B **85**, 075125 (2012).

[75] P. Schindler, D. Nigg, T. Monz, J. T. Barreiro, E. Martinez, S. X. Wang, S. Quint, M. F. Brandl, V. Nebendahl, C. F. Roos *et al.*, *A Quantum Information Processor with Trapped Ions*, New J. Phys. **15**, 123012 (2013).

[76] I. Pogorelov, T. Feldker, C. D. Marciniak, L. Postler, G. Jacob, O. Krieglsteiner, V. Podlesnic, M. Meth, V. Negnevitsky, M. Stadler, B. Hofer, C. Wachter, K. Lakhmanskiy, R. Blatt, P. Schindler, and T. Monz, *Compact Ion-Trap Quantum Computing Demonstrator*, PRX Quantum **2**, 020343 (2021).

[77] S. Kim, R. R. Mcleod, M. Saffman, and K. H. Wagner, *Doppler-Free, Multiwavelength Acousto-Optic Deflector for Two-Photon Addressing Arrays of Rb Atoms in a Quantum Information Processor*, Appl. Opt. **47**, 1816 (2008).

[78] P. Schindler, *Quantum Computation and Simulation with Trapped Ions Using Dissipation*, Ph.D. thesis, Universität Innsbruck, 2013.

[79] A. W. Cross, L. S. Bishop, J. A. Smolin, and J. M. Gambetta, *Open Quantum Assembly Language*, arXiv:1707.03429.

[80] D. C. McKay, C. J. Wood, S. Sheldon, J. M. Chow, and J. M. Gambetta, *Efficient Z Gates for Quantum Computing*, Phys. Rev. A **96**, 022330 (2017).

[81] F. Schmidt-Kaler, H. Häffner, S. Gulde, M. Riebe, G. Lancaster, J. Eschner, C. Becher, and R. Blatt, *Quantized AC-Stark Shifts and Their Use for Multiparticle Entanglement and Quantum Gates*, Europhys. Lett. **65**, 587 (2004).

[82] H. Häffner, S. Gulde, M. Riebe, G. Lancaster, C. Becher, J. Eschner, F. Schmidt-Kaler, and R. Blatt, *Precision Measurement and Compensation of Optical Stark Shifts for an Ion-Trap Quantum Processor*, Phys. Rev. Lett. **90**, 143602 (2003).

[83] D. Wineland, C. Monroe, W. Itano, D. Leibfried, B. King, and D. Meekhof, *Experimental Issues in Coherent Quantum-State Manipulation of Trapped Atomic Ions*, J. Res. Natl. Inst. Stand. Technol. **103**, 259 (1998).

[84] S. R. White, *Density Matrix Formulation for Quantum Renormalization Groups*, Phys. Rev. Lett. **69**, 2863 (1992).

[85] U. Schollwöck, *The Density-Matrix Renormalization Group in the Age of Matrix Product States*, Ann. Phys. (Amsterdam) **326**, 96 (2011).

[86] F. Verstraete, V. Murg, and J. Cirac, *Matrix Product States, Projected Entangled Pair States, and Variational Renormalization Group Methods for Quantum Spin Systems*, Adv. Phys. **57**, 143 (2008).

[87] J. I. Cirac, D. Pérez-García, N. Schuch, and F. Verstraete, *Matrix Product States and Projected Entangled Pair States: Concepts, Symmetries, Theorems*, Rev. Mod. Phys. **93**, 045003 (2021).

[88] I. H. Kim, *Noise-Resilient Preparation of Quantum Many-Body Ground States*, arXiv:1703.00032.

[89] T. Soejima, K. Siva, N. Bultinck, S. Chatterjee, F. Pollmann, and M. P. Zaletel, *Isometric Tensor Network Representation of String-Net Liquids*, Phys. Rev. B **101**, 085117 (2020).

[90] L. Slattery and B. K. Clark, *Quantum Circuits For Two-Dimensional Isometric Tensor Networks*, arXiv:2108.02792.

[91] Z.-Y. Wei, D. Malz, and J. I. Cirac, *Sequential Generation of Projected Entangled-Pair States*, Phys. Rev. Lett. **128**, 010607 (2022).

[92] Z.-Y. Wei, J. I. Cirac, and D. Malz, *Generation of Photonic Tensor Network States with Circuit QED*, Phys. Rev. A **105**, 022611 (2022).

[93] E. Martin-Lopez, A. Laing, T. Lawson, R. Alvarez, X.-Q. Zhou, and J. L. O'Brien, *Experimental Realization of Shor's Quantum Factoring Algorithm Using Qubit Recycling*, Nat. Photonics **6**, 773 (2012).

[94] R. Hooke and T. A. Jeeves, *"Direct Search" Solution of Numerical and Statistical Problems*, J. ACM **8**, 212 (1961).

[95] V. Torczon, *On the Convergence of Pattern Search Algorithms*, SIAM J. Optim. **7**, 1 (1997).

[96] C. E. Rasmussen and C. K. I. Williams, *Gaussian Processes for Machine Learning (Adaptive Computation and Machine Learning)* (MIT Press, Cambridge, MA, 2005).

[97] M. C. Fu, C.-H. Chen, and L. Shi, *Some Topics for Simulation Optimization*, in *Proceedings of the 2008 Winter Simulation Conference, Miami, FL, USA, 2008* (IEEE, New York, 2008), pp. 27–38.

[98] M. Riebe, K. Kim, P. Schindler, T. Monz, P. O. Schmidt, T. K. Körber, W. Hänsel, H. Häffner, C. F. Roos, and R. Blatt, *Process Tomography of Ion Trap Quantum Gates*, Phys. Rev. Lett. **97**, 220407 (2006).

[99] G. Kirchmair, J. Benhelm, F. Zähringer, R. Gerritsma, C. F. Roos, and R. Blatt, *Deterministic Entanglement of Ions in Thermal States of Motion*, New J. Phys. **11**, 023002 (2009).

[100] Z. Hradil, *Quantum-State Estimation*, Phys. Rev. A **55**, R1561 (1997).

[101] K. Banaszek, G. M. D'Ariano, M. G. A. Paris, and M. F. Sacchi, *Maximum-Likelihood Estimation of the Density Matrix*, Phys. Rev. A **61**, 010304(R) (1999).

[102] P. L. W. Maunz, *High Optical Access Trap 2.0.* (2016), 10.2172/1237003.

[103] T. Olsacher, L. Postler, P. Schindler, T. Monz, P. Zoller, and L. M. Sieberer, *Scalable and Parallel Tweezer Gates for Quantum Computing with Long Ion Strings*, PRX Quantum **1**, 020316 (2020).

[104] J. Carrasco, A. Elben, C. Kokail, B. Kraus, and P. Zoller, *Theoretical and Experimental Perspectives of Quantum Verification*, PRX Quantum **2**, 010102 (2021).

[105] A. Elben, R. Kueng, H. Y. R. Huang, R. van Bijnen, C. Kokail, M. Dalmonte, P. Calabrese, B. Kraus, J. Preskill, P. Zoller, and B. Vermersch, *Mixed-State Entanglement from Local Randomized Measurements*, Phys. Rev. Lett. **125**, 200501 (2020).

[106] S.-H. Lin, R. Dilip, A. G. Green, A. Smith, and F. Pollmann, *Real- and Imaginary-Time Evolution with Compressed Quantum Circuits*, PRX Quantum **2**, 010342 (2021).

[107] W. Huggins, P. Patil, B. Mitchell, K. B. Whaley, and E. M. Stoudenmire, *Towards Quantum Machine Learning with Tensor Networks*, Quantum Sci. Technol. **4**, 024001 (2019).

[108] A. Kandala, A. Mezzacapo, K. Temme, M. Takita, M. Brink, J. M. Chow, and J. M. Gambetta, *Hardware-Efficient Variational Quantum Eigensolver for Small Molecules and Quantum Magnets*, Nature (London) **549**, 242 (2017).

[109] H. L. Tang, V. O. Shkolnikov, G. S. Barron, H. R. Grimsley, N. J. Mayhall, E. Barnes, and S. E. Economou, *Qubit-ADAPT-VQE: An Adaptive Algorithm for Constructing Hardware-Efficient Ansätze on a Quantum Processor*, PRX Quantum **2**, 020310 (2021).

[110] M. Ostaszewski, L. M. Trenkwalder, W. Masarczyk, E. Scerri, and V. Dunjko, *Reinforcement Learning for Optimization of Variational Quantum Circuit Architectures*, arXiv:2103.16089.

[111] A. Sørensen and K. Mølmer, *Quantum Computation with Ions in Thermal Motion*, Phys. Rev. Lett. **82**, 1971 (1999).

[112] T. Choi, S. Debnath, T. A. Manning, C. Figgatt, Z.-X. Gong, L.-M. Duan, and C. Monroe, *Optimal Quantum Control of Multimode Couplings between Trapped Ion Qubits for Scalable Entanglement*, Phys. Rev. Lett. **112**, 190502 (2014).

[113] C. D. Marciniak, T. Feldker, I. Pogorelov, R. Kaubruegger, D. V. Vasilyev, R. van Bijnen, P. Schindler, P. Zoller, R. Blatt, and T. Monz, *Optimal Metrology with Programmable Quantum Sensors*, Nature (London) **603**, 604 (2022).

[114] C. Gardiner and P. Zoller, *The Quantum World of Ultra-Cold Atoms and Light Book II: The Physics of Quantum-Optical Devices* (World Scientific Publishing Company, Singapore, 2015), Vol. 4.

[115] F. Martínez-García, L. Gerster, D. Vodola, P. Hrmo, T. Monz, P. Schindler, and M. Müller, *Analytical and Experimental Study of Center-Line Miscalibrations in Mølmer-Sørensen Gates*, Phys. Rev. A **105**, 032437 (2022).

[116] L. Gerster, F. Martínez-García, P. Hrmo, M. W. van Mourik, B. Wilhelm, D. Vodola, M. Müller, R. Blatt, P. Schindler, and T. Monz, *Experimental Bayesian Calibration of Trapped-Ion Entangling Operations*, PRX Quantum **3**, 020350 (2022).

[117] J. Hilder, D. Pijn, O. Onishchenko, A. Stahl, M. Orth, B. Lekitsch, A. Rodriguez-Blanco, M. Müller, F. Schmidt-Kaler, and U. Poschinger, *Fault-Tolerant Parity Readout on a Shuttling-Based Trapped-Ion Quantum Computer*, arXiv:2107.06368.